A Momentum-conserving Accretion Disk Wind in the Narrow-line Seyfert 1 I Zwicky 1

J. N. Reeves[1,2] and V. Braito[1,2]

[1] Center for Space Science and Technology, University of Maryland Baltimore County, 1000 Hilltop Circle, Baltimore, MD 21250, USA; jreeves@umbc.edu
[2] INAF, Osservatorio Astronomico di Brera, Via Bianchi 46, I-23807 Merate (LC), Italy

Abstract

I Zwicky 1 (hereafter I Zw 1) is the prototype optical narrow-line Seyfert 1 galaxy. It is also a nearby ($z = 0.0611$), luminous quasi-stellar object (QSO), accreting close to the Eddington limit. *XMM-Newton* observations of I Zw 1 in 2015 reveal the presence of a broad and blueshifted P Cygni iron K profile, as observed through a blueshifted absorption trough at 9 keV and a broad excess of emission at 7 keV in the X-ray spectra. The profile can be well fitted with a wide-angle accretion disk wind, with an outflow velocity of at least $-0.25c$. In this respect, I Zw 1 may be analogous to the prototype fast wind detected in the QSO PDS 456, while its overall mass outflow rate is scaled down by a factor of 50, due to its lower black hole mass. The mechanical power of the fast wind in I Zw 1 is constrained to within 5%–15% of Eddington, while its momentum rate is of the order unity. Upper limits placed on the energetics of any molecular outflow, from its CO profile measured by IRAM, appear to rule out the presence of a powerful, large-scale, energy-conserving wind in this active galactic nucleus (AGN). We consider whether I Zw 1 may be similar to a number of other AGNs, such as PDS 456, where the large-scale galactic outflow is much weaker than what is anticipated from models of energy-conserving feedback.

Key words: black hole physics – galaxies: active – quasars: individual (I Zwicky 1) – X-rays: galaxies

1. Introduction

Ultrafast outflows were first detected through observations of blueshifted iron K-shell absorption profiles, as observed in the X-ray spectra of active galactic nuclei (AGNs). The first known examples of these fast outflows were discovered in the luminous quasars APM 08279+5255 (Chartas et al. 2002), PG 1211+143 (Pounds et al. 2003), and PDS 456 (Reeves et al. 2003). Since their initial discovery, a number of high column density ($N_H \sim 10^{23}$ cm^{-2}), ultrafast ($\sim 0.1c$) outflows have been found in luminous nearby AGNs (Tombesi et al. 2010; Gofford et al. 2013). These fast winds span a wide velocity range of up to $\sim 0.3c$, as seen in both PDS 456 (Matzeu et al. 2017) and the broad absorption-line quasar APM 08279+5255 (Saez & Chartas 2011).

One of the prototype ultrafast outflows occurs in the nearby ($z = 0.184$) quasi-stellar object (QSO) PDS 456. By utilizing the hard X-ray bandpass of *NuSTAR*, Nardini et al. (2015) revealed a blueshifted P Cygni profile at iron K in PDS 456, originating from a wide-angle accretion disk wind with an outflow velocity of up to $0.3c$. The mechanical power of these winds, like the one observed in PDS 456, can reach a significant fraction of the Eddington limit, which may be more than sufficient to provide the mechanical feedback required by models of black hole and host galaxy coevolution (Silk & Rees 1998; Fabian 1999; King 2003; Di Matteo et al. 2005; Hopkins & Elvis 2010). Such black hole winds may play a crucial part in regulating the growth of supermassive black holes and the bulges of their host galaxies in luminous QSOs. As black holes grow by accretion, strong nuclear outflows driven by the central AGN can potentially quench this process by shutting off their supply of matter, hereby setting the $M-\sigma$ relation that we see today (Ferrarese & Merritt 2000; Gebhardt 2000; Tremaine et al. 2002). In this scenario, gas swept up by the black hole wind within the host galaxy ISM can expand adiabatically, conserving energy in the process and helping to clear matter from the galaxy nucleus (Faucher-Giguère & Quataert 2012; Zubovas & King 2012; King & Pounds 2015).

AGN molecular gas outflows, observed on kiloparsec scales and with mass outflow rates up to or even exceeding 1000 M$_\odot$ yr^{-1}, may be the signature of this large-scale outflowing gas (Feruglio et al. 2010; Maiolino et al. 2012; Cicone et al. 2014, 2015; Fiore et al. 2017). A direct link between the inner, fast black hole winds and the large-scale molecular outflows was first made in the type II QSOs IRAS F11119 + 3257 (Tombesi et al. 2015) and Mrk 231 (Feruglio et al. 2015) via simultaneous detections of both blueshifted iron K absorption and blueshifted CO or OH profiles seen in the submillimeter band. In these AGNs, the momentum rate inferred for the molecular outflow was found to be boosted compared to the inner X-ray wind, consistent with the molecular outflow being driven by the energy-conserving feedback imparted by the initial black hole wind. A third example of a possible energy-conserving outflow was then found in the nearby narrow-line Seyfert 1 (NLS1) IRAS 17020+4544 (Longinotti et al. 2015, 2018). However, given the limited number of examples in AGNs to date, it is vital to explore further examples of fast disk winds, where their impact on larger scale gas can be directly assessed.

The subject of this paper is the nearby ($z = 0.0611$) NLS1 I Zwicky 1 (hereafter I Zw 1). I Zw 1 is the prototype optical NLS1, with strong Fe II emission and unusually narrow permitted lines, e.g., Hβ FWHM 1240 km s^{-1} (Sargent 1968; Osterbrock & Pogge 1985), and it is also a luminous radio-quiet PG QSO ($M_B = -23.5$; Schmidt & Green 1983). It is both a bright and rapidly variable X-ray source (Boller et al. 1996; Gallo et al. 2004; Wilkins et al. 2017). Previous *XMM-Newton* observations of I Zw 1 in 2002 and 2005 have shown the presence of a broad ionized emission line in the iron K band, which is centered nearer to 7 keV rather than the neutral Fe at 6.4 keV (Gallo et al. 2004, 2007; Porquet et al. 2004). This is also consistent with earlier measurements obtained by *ASCA* (Leighly 1999; Reeves & Turner 2000).

Table 1
Observation Log of I Zw 1

Start and End Date	Duration[a]	Net Exposure[b]
2002 Jun 22 09:18–2002 Jun 22 15:25	21.9	18.0
2005 Jul 18 15:22–2005 Jul 18 15:22	85.5	57.4
2015 Jan 19 08:56–2015 Jan 21 00:09	141.2	89.8
2015 Jan 21 09:20–2015 Jan 22 22:40	134. 4	78.3

Notes.
[a] Total duration of *XMM-Newton* observation, prior to screening.
[b] Net exposure of EPIC-pn detector after background screening and dead-time correction, in kiloseconds.

The bolometric luminosity of I Zw 1 is $L_{bol} \sim 3 \times 10^{45}$ erg s^{-1} (Porquet et al. 2004), which, for a black hole mass of $2.8^{+0.6}_{-0.7} \times 10^7 \, M_\odot$ (Vestergaard & Peterson 2006), implies that I Zw 1 accretes at close to the Eddington limit. Such high accretion rate AGNs may be prime candidates for driving a fast disk wind. Indeed, in addition to the X-ray winds observed in PG 1211+143 and IRAS 17020+4544, new examples of ultrafast outflows have also been measured in the NLS1s 1H 0707−495 (Kosec et al. 2018) and IRAS 13224−3809 (Parker et al. 2017; Pinto et al. 2018). Furthermore, the possible presence of an ultrafast wind in I Zw 1 has also been suggested by Mizumoto et al. (2019), who analyzed a small sample of X-ray observations of AGNs with existing constraints on the molecular outflow.

Motivated by this, here we present in detail the iron K-line profile obtained from all of the *XMM-Newton* observations of I Zw 1, and we report evidence for a fast ($\sim$0.25c) wide-angle wind, similar to the prototype example in PDS 456. We also compare the energetics derived from the iron K wind with constraints obtained from the submillimeter *IRAM* measurements in CO (Cicone et al. 2014) and demonstrate that the presence of a large-scale energy-conserving outflow appears to be ruled out in I Zw 1. In Section 2, we describe the *XMM-Newton* observations, while the iron K profile is analyzed in Section 3. In Section 4, the photoionization modeling of the fast outflow is discussed, while in Section 5 the wind profile is fitted with the accretion disk wind model of Sim et al. (2008, 2010). The energetics of the fast wind are calculated in Section 6, and these are subsequently compared to the molecular outflows observed in other AGNs.

2. Observations and Data Reduction

I Zw 1 was observed four times with *XMM-Newton* (see Table 1): in 2002 for about $\sim$22 ks, in 2005 for $\sim$86 ks, and more recently in 2015 in two consecutive orbits for $\sim$141 ks and $\sim$134 ks each. Each of the observations was processed and cleaned using the *XMM-Newton* Science Analysis Software (SAS, ver. 16.0.0) and the latest calibration files available. The resulting spectra were analyzed using the standard software packages (XSPEC ver. 12.9.1 and FTOOLS ver. 6.22). Here we concentrate on the data from the EPIC-pn camera, which, once cleaned for any high background, returned the net exposures listed in Table 1. Note the net exposures are also corrected for the dead time of the pn CCD camera. None of the observations was severely affected by high background, with only two minor flares during the last of the observations. All of the observations were performed with the thin filter applied and in small window mode, with the exception of the 2005

observation which was operating in the large window mode. The source spectra were extracted by adopting a circular region with a radius of 35″, while for the background spectra were extracted from two circular regions with radii of 23″, 35″, and 30″ for the 2002, 2005, and 2015 observations, respectively.

The two observations carried in 2015 were performed in the Reflection Grating Spectrometer (RGS) Multipointing Mode, which minimizes flux loss in the RGS at specific wavelengths that are caused by bad pixels or channels. This mode consists of splitting the observation into five different pointings, which have offsets in the dispersion direction of 0″, ±15″, and ±30″. Therefore, the EPIC observations also consist of five separate pointings, with total exposures ranging from $\sim$20 ks to $\sim$28 ks each. We treated each of the five EPIC-pn pointings separately, cleaning the background flares and extracting the source and background spectra. For each of the pointings we kept the same radius for the extraction regions and we generated the response matrices and the ancillary response files at the source position using the SAS tasks arfgen and rmfgen and the latest calibration available. We subsequently summed the five source and background spectra and combined the response matrices and ancillary response files with the appropriate weighting, which is proportional to the net exposure time of each of the pointings.

3. Spectral Analysis

We analyzed the two *XMM-Newton* spectra of I Zw 1 from 2015, using the EPIC-pn CCD detectors, concentrating on the 3–10 keV band in order to study the iron K profile from this AGN in detail. Note that I Zw 1 shows rapid X-ray variability on timescales of a few kiloseconds; e.g., see Figure 1, Wilkins et al. (2017). However, there was no significant variability of the Fe K profile on these timescales, and we proceeded to analyze the time-averaged spectra from each of the two *XMM-Newton* sequences. We limited the analysis to the higher energy band, noting that the soft X-ray spectrum below 3 keV shows a strong soft excess above the power-law continuum, while a warm absorber is present in I Zw 1 at lower energies. Note that the higher resolution soft X-ray spectra of I Zw 1 from the RGS on board *XMM-Newton* have been presented elsewhere. Silva et al. (2018) analyzed the RGS spectra from these 2015 observations, while Costantini et al. (2007) analyzed the RGS spectra from the earlier, shorter 2002 and 2005 *XMM-Newton* observations of I Zw 1. All of the soft X-ray spectra show the presence of a two-phase warm absorber, with outflow velocities of $\sim$2000 km s^{-1}. The warm absorber column densities from the 2015 spectra are of the order $N_H = 10^{21}$ cm^{-2} or lower and do not impact the hard X-ray spectrum above 3 keV.

The 3–10 keV pn spectra from each of the 2015 observations (OBS 1 and OBS 2) are plotted in Figure 1 (panel a), while the background spectra are also shown for comparison. Over the 3–10 keV band, the net source count rates are 0.388 ± 0.002 cts s^{-1} (OBS1) and 0.448 ± 0.003 cts s^{-1} (OBS 2), while the background rates are much lower with $1.53 \pm 0.04 \times 10^{-2}$ cts s^{-1} (OBS 1) and $2.92 \pm 0.06 \times 10^{-2}$ cts s^{-1}. As a result, the background level has little impact on the modeling of the spectrum over the Fe K band. Constant-energy bins were used for the spectral analysis, sampling the energy resolution of the EPIC-pn, which is $\sim$160 eV (FWHM) at 6 keV. The spectra have a minimum of 50 source counts per bin, enabling the use of χ^2 minimization in the spectral fitting. Note that all error measurements in the subsequent spectral
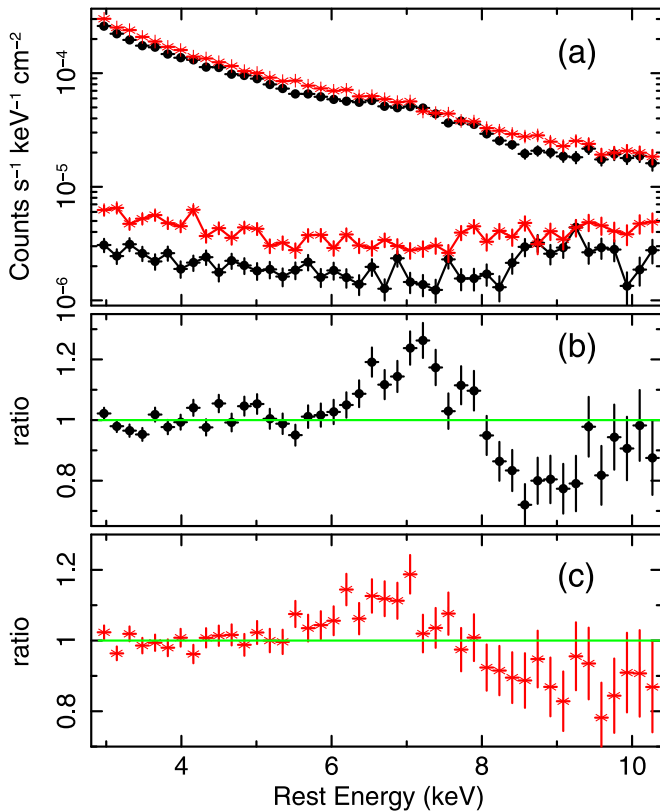
Figure 1. The 2015 *XMM-Newton* EPIC-pn spectra of I Zw 1. The OBS 1 sequence is shown in black; the OBS 2 sequence in red. The plot is the QSO rest frame at $z = 0.0611$. The upper panel (a) shows the net count rate spectra for both observations, while the lower points show the level of the background, which lies well below the spectra. The overall flux of the OBS 2 spectrum is about 10% higher than that of OBS 1. The lower panels show the data/model ratio of these spectra to a simple power-law model of photon index $\Gamma = 2.13 \pm 0.03$, whereby the OBS 1 spectrum is shown in panel (b) and the OBS 2 spectrum is shown in panel (c). A broad emission component is present in the residuals, peaking at around 7 keV, likely arising from ionized iron. At higher energies, a broad absorption trough is present above 8 keV. The residuals appear to be stronger in the lower flux OBS 1 spectrum and shallower in OBS 2.

Table 2
Iron K Profile Parameters for I Zw 1

	OBS 1	OBS 2
Gaussian emission:		
$E_{\rm rest}$[a]	$7.05^{+0.21}_{-0.19}$	$7.05^{\rm t}$
σ[b]	$0.66^{+0.17}_{-0.16}$	$0.94^{+0.19}_{-0.17}$
Normalization[c]	$1.85^{+0.78}_{-0.54}$	$1.31^{+0.75}_{-0.47}$
Line flux[d]	$2.1^{+0.9}_{-0.6}$	$1.5^{+0.8}_{-0.5}$
EW[e]	390^{+160}_{-110}	240^{+140}_{-90}
$\Delta\chi^2$[f]	119.3	⋯
Gaussian absorption:		
$E_{\rm rest}$[a]	$8.66^{+0.20}_{-0.22}$	$8.66^{\rm t}$
σ[b]	$0.66^{\rm t}$	$0.94^{\rm t}$
Normalization[c]	$-1.28^{+0.37}_{-0.45}$	$-1.05^{+0.42}_{-0.50}$
Line flux[d]	$-1.8^{+0.5}_{-0.6}$	$-1.5^{+0.6}_{-0.7}$
EW[e]	-410^{+120}_{-140}	-290^{+120}_{-140}
$\Delta\chi^2$[f]	62.2	⋯
Continuum:		
Γ	2.14 ± 0.04	$2.14^{\rm t}$
$F_{\rm 2-10\,keV}$[g]	5.22	6.04
χ^2_ν[h]	81.8/81	
P Cygni:		
E_0[a]	7.3 ± 0.1	$7.1^{+0.1}_{-0.2}$
α_1	$1.9^{+1.6}_{-1.1}$	$1.9^{\rm t}$
v_∞/c	$-0.35^{+0.03}_{-0.04}$	<-0.39
$\tau_{\rm tot}$	$0.19^{+0.05}_{-0.04}$	$0.11^{+0.03}_{-0.03}$
$N_{\rm H}$[i]	6.3 ± 1.6	3.8 ± 1.3
χ^2/ν[h]	78.5/80	

Notes.
[a] Rest-frame centroid energy in keV.
[b] Gaussian width in keV.
[c] Gaussian normalization (photon flux) in units of 10^{-5} photons cm^{-2} s^{-1}.
[d] Line flux in units of 10^{-13} erg cm s^{-1}.
[e] Equivalent width in eV.
[f] Improvement in χ^2 upon adding component to model.
[g] Observed 2–10 keV flux in units of 10^{-12} erg cm^{-2} s^{-1}.
[h] Reduced chi-squared for fit.
[i] Hydrogen column density in units of 10^{-23} cm^{-2}, calculated from the profile optical depth ($\tau_{\rm tot}$).
[t] Denotes parameter is tied in fit.

fitting are given at the 90% confidence level for one parameter of interest.

The OBS 1 and OBS 2 spectra were fitted simultaneously with a simple power-law continuum, allowing its normalization to vary between the two observations to account for the variation in overall flux, but linking the photon index between them, with $\Gamma = 2.13 \pm 0.03$. A neutral Galactic column of $N_{\rm H} = 6.0 \times 10^{20}$ cm^{-2} (Kalberla et al. 2005) was also included. The fit to this simple model is very poor with $\chi^2_\nu = 263.7/87$, rejected with a null hypothesis probability of $P_{\rm N} = 1.1 \times 10^{-19}$. Panels (b) and (c) show the data/model ratio residuals to this power law, which show strong residuals in the Fe K band. A broadened emission line is present near 7 keV in both data sets, while at higher energies above 8 keV, a broad absorption trough is also present. Comparison between the residuals of the two spectra shows that the line residuals appear to be somewhat stronger in the lower flux OBS 1 spectrum and somewhat shallower (or broader) in OBS 2.

3.1. Gaussian Fe K Profile

To provide an initial parameterization of the Fe K profile, a double-Gaussian profile was fitted to the data sets to account for

both the excess emission as well as the absorption trough, where the latter is allowed to have a negative normalization. The line widths of the emission versus absorption components were assumed to be the same for simplicity, although the overall width was allowed to vary between the OBS 1 and OBS 2 spectra to account for any profile variability. The line normalizations were also allowed to vary; however, the centroid energies of the emission and absorption components were tied between the OBS 1 and OBS 2 spectra to reduce any parameter degeneracy.

The fit parameters to the Gaussian model are tabulated in Table 2. The addition of both lines significantly improved the fit by $\Delta\chi^2 = -119.3$ and $\Delta\chi^2 = -62.2$ for the emission and absorption, respectively, while the overall fit statistic was reduced to an acceptable $\chi^2_\nu = 81.8/81$. The best-fit Gaussian profiles are shown in Figure 2 (panel a), superimposed on the fluxed spectra for OBS 1 and OBS 2.[3] The Gaussian profiles

---

[3] The fluxed spectra in this paper are created using an input count rate spectrum (units of counts s^{-1} keV^{-1} cm^{-2}), which is folded by the instrumental response, but has been divided through by the instrumental effective area (using the SETPLOT AREA command within XSPEC). The y-axis values are then multiplied twice by energy and by a conversion factor of 1 keV $= 1.602 \times 10^{-9}$ erg to convert the spectrum into νF_ν flux units.
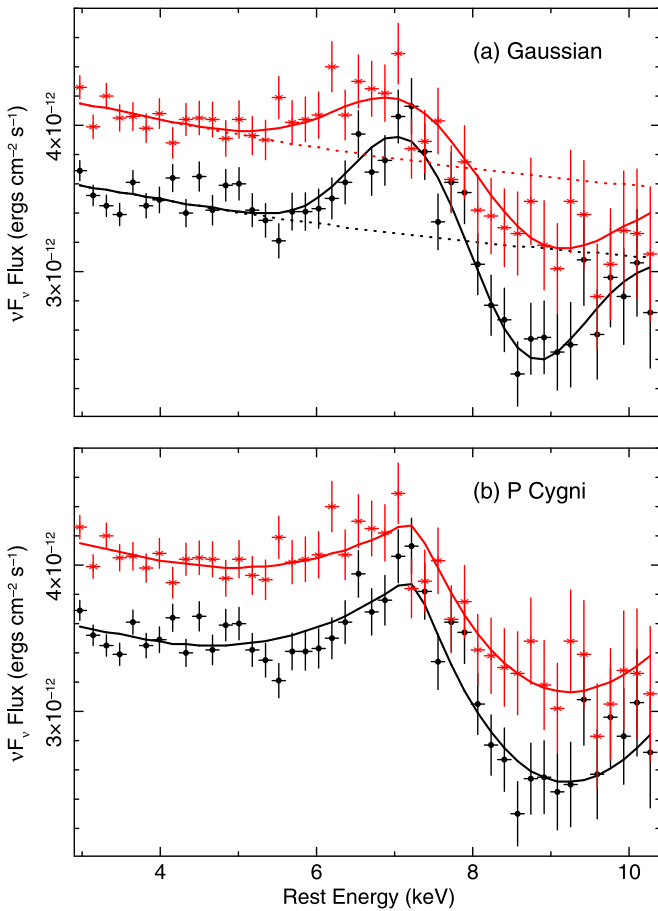
Figure 2. Fluxed spectra of I Zw 1 fitted with two profiles, (a) a Gaussian profile in emission and absorption and (b) a P Cygni wind profile. OBS 1 spectra are in black and OBS 2 spectra in red. The Gaussian profile in panel (a) clearly shows the broadened emission vs. blueshifted absorption in the iron K band, while the best-fitting power-law continuum is shown as a dashed line. The best-fit centroid energy of the blueshifted absorption trough, near 8.6 keV, when compared to the expected energies of He- or H-like iron (6.70 or 6.97 keV), indicate the presence of a fast wind. The P Cygni profile in panel (b) is fitted with the model of Done et al. (2007) from a spherical wind reaching a terminal velocity of $v_\infty \sim 0.35c$. See Section 3 and Table 2 for details of the model parameters.

returned rest-frame centroid energies of $E = 8.66^{+0.20}_{-0.22}$ keV in absorption and $E = 7.05^{+0.21}_{-0.29}$ keV for the emission. The centroid energy of the absorption trough implies it is substantially blueshifted if it is associated with the strong $1s \rightarrow 2p$ lines of highly ionized iron. Compared to the expected lab frame energies of the He-like Fe XXV resonance line (at 6.7 keV) or the H-like Fe XXVI Lyα line (at 6.97 keV), the corresponding outflow velocities are $v/c = -0.24 \pm 0.02$ and $v/c = -0.21 \pm 0.02$, respectively. On the other hand, the centroid of the emission is consistent with an origin from H-like iron. The profile is also broadened, with a best-fit Gaussian width of $\sigma = 660^{+170}_{-160}$ eV for OBS 1 versus $\sigma = 940^{+190}_{-170}$ eV for OBS 2. However, given the errors, the difference in velocity width between the profiles is only significant at about the 90% confidence level, and both profiles can also be adequately fitted with a common velocity width, of $\sigma = 770 \pm 160$ eV. Note that this line width, with respect to the emission centroid at 7 keV, corresponds to a velocity broadening of $\sigma_v = 33{,}000$ km s^{-1} (or $0.11c$). Overall, the profile appears very reminiscent of the broad, P-Cygni-like

profile measured from the fast wind in PDS 456 (Nardini et al. 2015).

Notably, the equivalent widths of the emission versus absorption components are roughly equal; for instance, during OBS 1 the equivalent width of the emission line (390^{+160}_{-110} eV) is similar to the absorption trough (-410^{+120}_{-140} eV), while in OBS 2 the equivalent widths are slightly smaller (see Table 2). If the emission originates via reemission from a wind, this implies that the geometrical covering of the wind is relatively high, as most of the continuum photons that are absorbed by material covering a substantial fraction of 4π steradians are subsequently reemitted. On the other hand, if the absorbing gas was isolated to a relatively small clump of material located only along the line of sight, then its total emission would be relatively small, and the Fe K profile would be narrow. We explore this further below, where we model the Fe K profile with a P Cygni profile from a near-spherical wind.

3.1.1. Comparison with EPIC-MOS

The spectra obtained from the EPIC-MOS cameras were also checked for consistency with the EPIC-pn. After the individual MOS 1 and MOS 2 spectra were found to be consistent, these were combined into a single MOS spectrum for each observation, after combining the response files with the appropriate weighting. Figure 3 shows the resulting MOS spectrum for OBS 1 versus the pn spectrum, where the upper panel shows a ratio to a simple power-law model. Both spectra are clearly consistent with each other, with the MOS data also showing both the broad emission component centered near 7 keV and a broad blueshifted absorption trough near 9 keV. A joint fit between the pn and MOS spectra for OBS 1 yielded consistent result compared to the above, where for the absorption line $E = 8.7 \pm 0.2$ keV, $\sigma = 635 \pm 150$ eV and EW $= -360 \pm 85$ eV, with consistent parameters also obtained for the broad ionized emission. No further residuals are present in either the pn or MOS spectra at iron K once these Gaussian components are included in the model (see lower panel of Figure 3). Likewise the MOS spectra for OBS 2 are also consistent with the pn. Thus, both the pn and MOS data verify the presence of the blueshifted absorption in I Zw 1.

We also attempted to place limits on any narrow Fe Kα emission in the I Zw 1 spectra. Narrow components of the 6.4 keV Fe Kα fluorescence line appear to be almost ubiquitous in the X-ray spectra of Seyfert galaxies (e.g., Nandra et al. 2007) and may originate from X-ray reflection off distant Compton-thick matter, such as a parsec-scale molecular torus (Ikeda et al. 2009; Murphy & Yaqoob 2009; Brightman & Nandra 2011). The simultaneous pn and MOS spectra for each observation were used to place a limit on the narrow iron Kα component at 6.4 keV. As can be seen in Figure 3 (lower panel), once the broad ionized emission and absorption lines are included in the model, there are no residuals apparent near 6.4 keV in either the pn or MOS spectra. To calculate an upper limit on the equivalent width, a narrow Gaussian was included with a fixed width of $\sigma = 10$ eV, while the centroid energy of the Gaussian was restricted to be within ± 0.1 keV of 6.4 keV. A best-fit continuum model consisting of a power law and the two broad Gaussians was adopted, allowing the fit parameters to adjust accordingly. A tight upper limit on the equivalent width of EW < 30 eV was found for OBS 1, while for OBS 2 the upper limit is lower still, with EW < 18 eV. Thus, as the
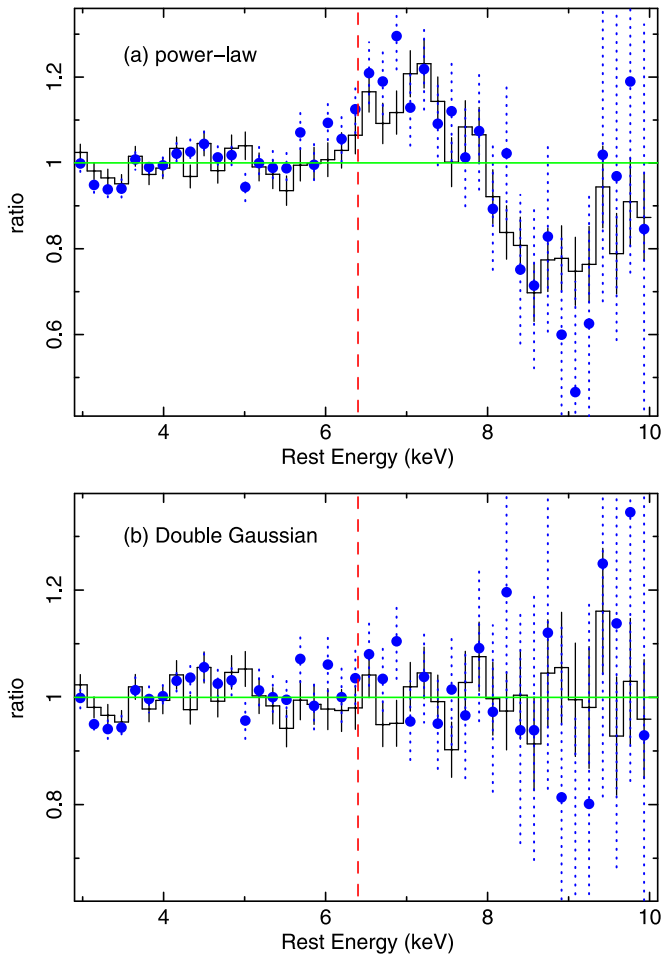
Figure 3. Comparison between the pn and MOS spectra for OBS 1, where the pn data are in black and the MOS data are shown as blue circles. The upper panel shows the ratio of the spectra compared to a power law with Galactic absorption. The broad Fe K emission line and blueshifted absorption feature, centered near 7 keV and 9 keV, respectively, are detected independently in the MOS spectra, and the overall profile is consistent between the pn and MOS. Note that both data sets are binned to constant-energy bins of $\Delta E = 160$ eV, at approximately the FWHM resolution. The lower panel shows the residuals after the broad Gaussian absorption and emission components have been added to the model. Note the dashed red line marks the expected position of a neutral Fe Kα line, which is not observed in the spectra.

contribution of a distant reflection component, via the neutral Fe Kα line, appears negligible in I Zw 1, it has not been included in any of the subsequent modeling.

The weakness of the narrow Fe Kα line in I Zw 1 might be explained by the X-ray Baldwin effect, where the equivalent width of the narrow Fe Kα line is observed to decrease with increasing AGN X-ray luminosity (Iwasawa & Taniguchi 1993; Nandra et al. 1997; Reeves & Turner 2000; Page et al. 2005; Bianchi et al. 2007). Note that for the 2–10 keV luminosity of I Zw 1 of $L_{2-10\,\mathrm{keV}} = 5 \times 10^{43}$ erg s^{-1}, Bianchi et al. (2007) predicted an equivalent width in the range of 40–90 eV (see their Figure 1) and thus the above upper limits are somewhat lower than expected. For the likely black hole mass and bolometric luminosity of I Zw 1, then its Eddington ratio is of the order $L_{\mathrm{bol}}/L_{\mathrm{Edd}} \sim 1$. From the anticorrelation in Bianchi et al. (2007) between the Fe Kα equivalent width and Eddington ratio, the predicted equivalent width is 20–70 eV, which is consistent with the limits observed. Thus, the high

Eddington ratio of I Zw 1 might explain the weakness of its narrow Fe Kα line.

3.2. P Cygni Profile

Because the observed profiles are reminiscent of the classical P-Cygni-like profile, we tested the same customized model for a P Cygni profile that was applied by Nardini et al. (2015) to PDS 456. The model was developed for the Fe K absorption feature seen in 1H 0707−495 (Done et al. 2007) and is based on the Sobolev approximation with exact integration (SEI) for a spherically symmetric wind. The parameters of the model are the energy of the onset of the absorption component (E_0), the terminal velocity of the wind (v_∞), how the velocity scales with distance (γ), the initial velocity at the photosphere (w_0), and the optical depth (τ_{tot}) and the smoothness of the profile. The smoothness is defined by two parameters α_1 and α_2, where higher values correspond to smoother profiles. The velocity field is defined by $w = w_0 + (1 - w_0)(1 - 1/x)^\gamma$, where $w = v/v_\infty$ is the ratio between the wind velocity and the terminal velocity v_∞, w_0 is the initial velocity at the photosphere, and $x = r/R_0$ is the radial distance in units of photospheric radius. At large radii, where $r \gg R_0$, the wind velocity tends to $v = v_\infty$. Following Nardini et al. (2015), we adopted $\gamma = 1$ and $w_0 = 0.01$, as they have a marginal effect on the profile, with these parameters the line optical depth varies as

$$\tau(w) \propto \tau_{\mathrm{tot}}\, w^{\alpha_1}(1 - w)^{\alpha_2}. \qquad (1)$$

We then replaced the two Gaussians with the P Cygni model and fitted simultaneously OBS 1 and OBS 2. The pn spectra were used as these yield the highest signal-to-noise ratio at high energies, but noting the consistency with the MOS. We tied the underlying continuum slope but allowed the normalizations to vary. Regarding the P Cygni parameters, we allowed the optical depths, the terminal velocities, and the rest-frame energies of the P Cygni line, E_0, to vary independently, in order to account for changes in the profiles and their intensities. We assumed that $\alpha_1 = \alpha_2 = \alpha$, as they cannot be constrained separately. This results in a symmetrical absorption profile, where the trough minimum (at maximum τ) occurs at $v_\infty/2$. As expected from the earlier Gaussian profile, the P Cygni model results in a good fit ($\chi^2/\nu = 78.5/80$). The best-fit parameters are reported in Table 2. Note that similar to the Gaussian model, the P Cygni model results in a marginally shallower profile during OBS 2, where we found that the optical depth marginally decreases from $\tau_{\mathrm{tot}} = 0.19^{+0.05}_{-0.04}$ (OBS 1) to $\tau_{\mathrm{tot}} = 0.11^{+0.03}_{-0.03}$ (OBS 2). We can only place a lower limit to the terminal velocity ($v_\infty/c < -0.39$) during OBS 2, while during OBS 1 we derive a terminal velocity of $v_\infty/c = -0.35^{+0.03}_{-0.04}$.

From the optical depth (τ_{tot}), we can derive an estimate of the ionic column density of the gas through the relation $\tau_{\mathrm{tot}} = (\pi e^2/m_e\, c)f\lambda_0 N_i/v_\infty$, where m_e and e are the electron mass and charge (in statcoulombs), λ_0 (in centimeters) is the wavelength of the line (lab frame), and f is the oscillator strength of the transition. Now, assuming an identification with Fe XXVI Lyα ($f = 0.21$), we derive ionic columns of $N_i = (2.0 \pm 0.5) \times 10^{19}$ cm^{-2} and $N_i = (1.2 \pm 0.4) \times 10^{19}$ cm^{-2} for OBS 1 and OBS 2, respectively. Thus, for the solar abundances of Grevesse & Sauval (1998), these correspond to $N_H = (6.3 \pm 1.6) \times 10^{23}$ cm^{-2} and $N_H = (3.8 \pm 1.3) \times 10^{23}$ cm^{-2} for OBS 1 and OBS 2.
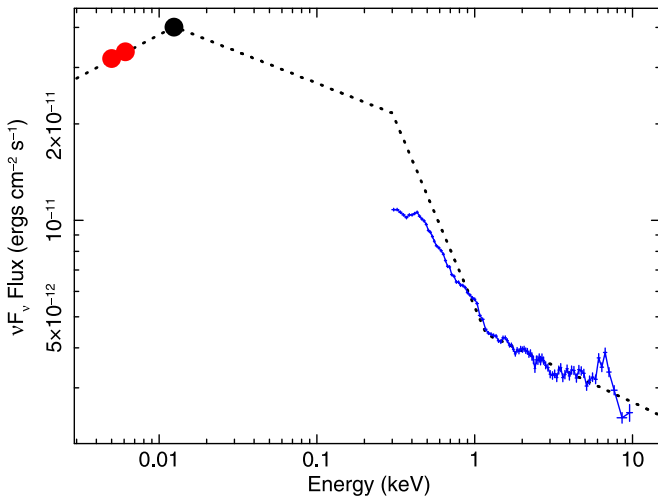
Figure 4. The UV to X-ray SED of I Zw 1, taken from the 2015 *XMM-Newton* observations. The EPIC-pn spectrum (from OBS 1) is shown in blue, while UV photometric points from the UVW1 and UVW2 filters from the *XMM-Newton* OM are shown as red circles. Note that the black circle shows the nonsimultaneous measurement from *FUSE* in the far-UV (Scott et al. 2004). The UV and X-ray data are corrected for reddening and Galactic absorption, respectively. The dashed line shows the phenomenological model fitted to the SED and corrected for intrinsic X-ray absorption. This consists of a series of power-law portions, with three break points, at 12.5 eV, 300 eV, and 1.2 keV; see Section 4.2 for details.

4. Photoionization Modeling

4.1. The Photoionizing Continuum

We next modeled the *XMM-Newton* spectrum with a self-consistent photoionization model, using the XSTAR code (Kallman et al. 2004). The UV to X-ray SED of I Zw 1 was used to estimate the input photoionizing continuum, which is plotted in Figure 4 for the 2015 epoch (for simplicity we only used the OBS 1 sequence). Simultaneous UV photometry from the UVW1 and UVW2 filters from the Optical Monitor (OM) on board *XMM-Newton*, along with the 0.3–10 keV EPIC-pn spectrum, was used. In addition, we adopted an earlier nonsimultaneous data point from *FUSE* in the far-UV at ~1000 Å (Scott et al. 2004) in order to anchor the UV continuum, noting that the FUSE data point lies on the extrapolation of the UV continuum in Figure 4. All data points have been corrected for Galactic extinction of $E(B-V) =$ 0.057, while the X-ray data points are corrected for Galactic photoelectric absorption, corresponding to a column of $N_H = 6 \times 10^{20}$ cm^{-2} and solar abundances of Grevesse & Sauval (1998).

The SED is parameterized by a series of power laws, with three break points. Below 12.5 eV in the UV, the OM and *FUSE* points are connected by a photon index of $\Gamma_{UV} = 1.75$, while the far-UV to soft X-ray (from 12.5 to 300 eV) bands are connected by $\Gamma_{UVX} = 2.2$. From 0.3 to 1.2 keV, the soft X-ray spectrum is modeled by a steep photon index of $\Gamma_{SX} = 3.3 \pm 0.2$ to approximate the soft excess, while a photon index of $\Gamma_X = 2.21 \pm 0.03$ describes the hard X-ray power law above a break energy of 1.2 keV. Note that the opacity due to the warm absorber, as modeled by a two-phase model in Silva et al. (2018), has been accounted for in determining the soft X-ray continuum. From this SED, the subsequent ionizing (1–1000 Ryd) luminosity is estimated to be $L_{ion} \sim 1.5 \times 10^{45}$ erg s^{-1}. This is likely to be a relatively conservative estimate for the ionizing luminosity, which could be somewhat higher, e.g., if the SED peaks in between the observable UV and soft X-ray bands. If we adopted a higher break energy of 100 eV (instead of 12.5 eV) for the first break point between the UV and soft X-rays, then the 1–1000 Ryd band luminosity is slightly higher (3×10^{45} erg s^{-1}). We note that Porquet et al. (2004) also estimated a total bolometric luminosity of 3×10^{45} erg s^{-1}, based on scaling the 5100 Å flux, which is close to the Eddington value for the black hole mass of I Zw 1.

Regardless of the exact parameterization of the overall SED, the most critical parameter for the photoionization modeling is the X-ray photon index above 1 keV, which sets the ionization balance for the highly ionized iron K-shell lines. Thus, if the X-ray continuum was much harder ($\Gamma < 2$) than that observed here, then the number of ionizing photons above the Fe K edge threshold at 7.11 keV would be greater and the Fe K features will be subsequently more ionized and weaker, as more ions become fully ionized. Future observations with *NuSTAR* will be able to determine the exact form and slope of the continuum above 10 keV, although the pn spectra suggest a steep hard X-ray slope with $\Gamma = 2.1$–2.2.

4.2. Photoionization Results

Grids of photoionization models were subsequently generated within XSTAR for the spectral fitting, using the above SED as the input continuum. The absorption was accounted for by a multiplicative grid, while the emission from the wind was modeled by an additive grid. A velocity broadening of $b = 25,000$ km s^{-1} was used in the models, accounted for by the turbulence velocity parameter[4] and is consistent with the line widths inferred from the earlier Gaussian analysis. Solar abundances of Grevesse & Sauval (1998) were used throughout. The overall form of the model is

$$\text{tbabs} \times (\text{xstar}_{abs} \times \text{pow} + \text{xstar}_{emiss}), \qquad (2)$$

where xstar$_{abs}$ denotes the iron K absorption and xstar$_{emiss}$ represents the photoionized emission. The spectra are absorbed by a Galactic component of absorption, via the TBABS model (Wilms et al. 2000), as above. Note that we allowed the column density to vary between the OBS 1 and OBS 2 spectra, but tied the ionization and outflow velocity between them, which otherwise were consistent within errors. We assumed the column density of the emission component (as well as its ionization) to be the same as that of the absorber, and these were subsequently tied. Note that the net outflow velocity of the emitter was not tied to that of the absorber. In this case, no strong net blueshift was required for the emitter, with an upper limit of $v < 0.05c$ and thus was subsequently fixed at zero. We note that in the case of a wide-angle wind, the observed emission can be observed over all angles, and thus a net blueshift of the emission need not be observed. In this respect, both the P Cygni model and the disk wind model of Sim et al. (2008, 2010) investigated later (see Section 5) self-consistently calculate the expected velocity profiles for a spherical and biconical wind geometry, respectively.

The best-fit parameters of the photoionized emission and absorption model are shown in Table 3, and overall, the fit

---

[4] Within XSTAR, the turbulence velocity is defined as $b = \sqrt{2}\sigma = \text{FWHM}/(2\sqrt{\ln 2})$.

Table 3
Photoionization Modeling of the Wind

Parameter	2015 OBS 1	2015 OBS 2	2002	2005
Fe K absorber:				
N_H [a]	$7.5^{+1.4}_{-1.2}$	$4.5^{+1.4}_{-1.1}$	$4.8^{+2.3}_{-2.0}$	$2.0^{+1.2}_{-1.1}$
$\log \xi$ [b]	$4.91^{+0.37}_{-0.13}$	4.91^{t}	4.9^{f}	5.0^{t}
v/c	-0.265 ± 0.010	-0.265^{t}	-0.29 ± 0.03	-0.25 ± 0.02
F_{abs} [c]	$4.0^{+0.7}_{-0.6}$	$2.9^{+0.9}_{-0.7}$	$4.7^{+2.0}_{-1.7}$	<0.95
Fe K emission:				
N_H [a]	7.5^{t}	4.5^{t}	4.8^{t}	$4.6^{+1.7}_{-1.3}$
$\log \xi$ [b]	4.91^{t}	4.91^{f}	4.9^{f}	$5.0^{+0.5}_{-0.4}$
F_{emiss} [c]	$1.9^{+0.6}_{-0.4}$	$1.3^{+0.6}_{-0.5}$	<4.1	$1.8^{+0.7}_{-0.5}$
κ [d]	$3.7^{+1.2}_{-0.9} \times 10^{-4}$	$4.2^{+2.2}_{-1.8} \times 10^{-4}$	$<8.2 \times 10^{-4}$	5×10^{-4f}
$f = \Omega/4\pi$ [d]	$0.71^{+0.23}_{-0.17}$	$0.81^{+0.19}_{-0.35}$	...	1.0^{f}
Continuum:				
Γ	2.15 ± 0.03	2.15^{f}	2.22 ± 0.07	2.10 ± 0.05
$F_{2-10\,keV}$ [e]	5.24	6.08	8.47	5.01

Notes.
[a] Units of column density $\times 10^{23}$ cm^{-2}.
[b] Ionization parameter (where $\xi = L/nR^2$) in units of erg cm s^{-1}.
[c] Flux absorbed from the continuum or reemitted over the Fe K band, in units of 10^{-13} erg cm^{-2} s^{-1}.
[d] Fitted normalization of the XSTAR emission component, where $\kappa = f L_{38}/D_{kpc}^2$ and $f = \Omega/4\pi$ is the emitter covering fraction, L_{38} is the 1–1000 Ryd ionizing luminosity in units of 10^{38} erg s^{-1}, and D_{kpc} is the distance to I Zw 1 in units of kiloparsecs.
[e] Observed 2–10 keV flux, not corrected for absorption, in units of 10^{-12} erg cm^{-2} s^{-1}.
[f] Denotes parameter is fixed.
[t] Denotes parameter is tied between observations.

statistic is good, with $\chi^2_\nu = 71.8/81$. Removing either the absorption or emission from the model results in a substantially worse fit, with $\Delta\chi^2 = 91$ for $\Delta\nu = 3$ for the absorber versus $\Delta\chi^2 = 101$ for $\Delta\nu = 3$ for the emission. Figure 5 shows the best-fit XSTAR model fitted to both spectra, which can well reproduce both the emission and absorption from the wind. The column density from the OBS 1 spectrum ($N_H = 7.5^{+1.4}_{-1.2} \times 10^{23}$ cm^{-2}) was found to be slightly higher than that for OBS 2 ($N_H = 4.5^{+1.4}_{-1.1} \times 10^{23}$ cm^{-2}), which is consistent with the absorption trough being deeper in OBS 1. These column densities are also consistent with what was derived from the earlier P Cygni profile results. The ionization of the gas is high, with $\log \xi = 4.91^{+0.37}_{-0.13}$, with the absorption and emission mainly arising from He- and H-like iron. The outflow velocity of the absorber was $-0.265 \pm 0.010c$, while no significant velocity shift was required in emission. Note that the outflow velocity derived from the XSTAR model is slightly lower than the terminal velocity obtained from the P Cygni model, as it is calculated from the centroid of the absorption profile rather than from its maximum bluewards extent.

The geometrical covering fraction of the gas f was also calculated from the normalization of the XSTAR emission component κ, where:-

$$\kappa = f \times \frac{L_{38}}{D_{kpc}^2}. \quad (3)$$

Here, L_{38} is the 1–1000 Rydberg ionizing luminosity and D_{kpc} is the luminosity distance to the source in kiloparsecs, while $f = 1$ for a fully covering spherical shell of gas. Thus, from the measured normalizations reported in Table 1 and adopting $D = 240$ Mpc and $L = 3 \times 10^{45}$ erg s^{-1} for I Zw 1, the covering fraction was estimated to be $f = 0.71^{+0.23}_{-0.17}$ and $f = 0.81^{+0.19}_{-0.35}$ for OBS 1 and OBS 2, respectively. The gas
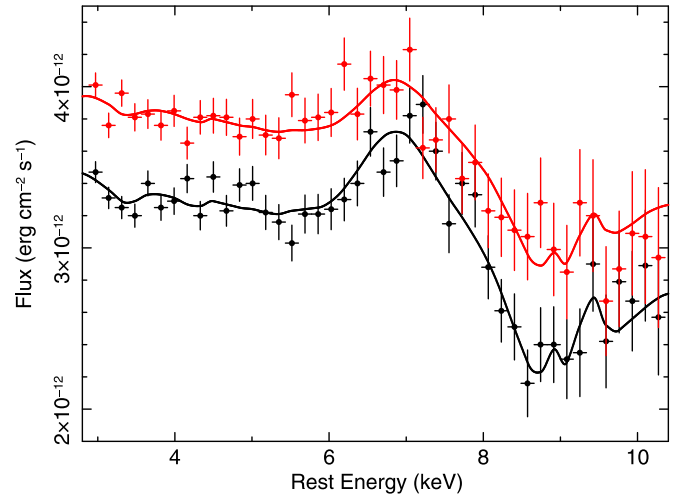
Figure 5. The 2015 pn spectra of I Zw 1, fitted with the XSTAR model described in Section 4.2 and with the parameters listed in Table 3. The emission and absorption model applied to the data has a velocity broadening of 25,000 km s^{-1}, in order to account for the profile width. A fast absorber, of outflow velocity $v/c = -0.265 \pm 0.010$, accounts for the broad absorption trough, while the iron K emission results from the subsequent reemission from the wind. Note the very weak emission feature at 9.3 keV is the radiative recombination emission from Fe XXVI.

covering can also be estimated by comparing the flux absorbed from the continuum with what is reemitted over the iron K band in the form of line emission, where a ratio close to 1 might be expected for a fully covering wind. These values are reported in Table 1, which shows that about half of the incident radiation that is absorbed is subsequently reemitted. Thus, the wind is likely to cover at least 2π steradians solid angle with respect to the X-ray continuum source.

4.3. Alternative Reflection Models

We also tested whether the Fe K profile of I Zw 1 could be fitted with relativistically blurred reflection instead of a wind, which then could originate off the surface of the inner accretion disk. Initially, a model with no wind absorption was tested, simply consisting of an ionized blurred reflection component and a power-law continuum, which are absorbed only by the Galactic absorption. To model the reflection, the XILLVER emission table was used (García et al. 2013), which was convolved with a relativistic blurring kernel, KDBLUR, which approximates the disk emissivity versus radius with a simple power-law function as R^{-q}. The inner disk radius was initially fixed to the innermost radius expected from around a maximal Kerr black hole (with $R_{in} = 1.24R_g$), while the outer radius was fixed to $R_{out} = 400R_g$. The iron abundance of the reflector was assumed to be solar, which is otherwise poorly constrained with an upper limit of $A_{Fe} < 5$. The continuum incident upon the reflector was assumed to have the same photon index as the primary power law, while the high-energy cutoff was fixed at 300 keV, as this cannot be constrained without hard X-ray data. The normalization and ionization of the reflector was allowed to vary, as well as the disk inclination and emissivity index, while the power-law photon index and normalization were allowed to vary for both observations. However, this reflection model resulted in a rather poor fit, with $\chi_\nu^2 = 125.2/79$, and the model left significant residuals above 8 keV, due to the presence of the blueshifted absorption.

Thus, the input model was adjusted to include the photoionized absorption from the wind, as well as the reflected emission from the accretion disk. The form of the model is then

$$\text{tbabs} \times (\text{xstar}_{abs} \times \text{pow} + \text{kdblur} \otimes \text{xillver}). \qquad (4)$$

Note that this is phenomenologically identical to the above XSTAR emission plus absorption model, except the photoionized emission has been replaced by the ionized reflector (XILLVER), which is convolved with KDBLUR to account for the line broadening. This model then provided an acceptable fit, where $\chi_\nu^2 = 73.3/76$, and it appears identical to that in Figure 5, The wind parameters remained unchanged within errors from before; e.g., for OBS1 for an absorber ionization of $\log \xi = 5$, the column density is $N_H = 6.8^{+4.2}_{-2.3} \times 10^{23}$ cm^{-2}, with an outflow velocity of $v = -0.24 \pm 0.01c$. The ionization of the reflector is $\log \xi = 3.1 \pm 0.3$, while the inclination is also quite high, with $\theta = 58^{+15}_{-8}°$ in order to match the centroid energy of the broad emission component. The emissivity index is relatively flat, with $q = 2.2^{+0.6}_{-0.5}$, which suggests that the X-ray emission is not highly centrally concentrated close to the black hole, as is evidenced by the relative lack of a strong red wing to the iron K profile (see Figure 3). Indeed, only an upper limit of $R_{in} < 16R_g$ can be placed on the inner disk radius in this case. In this model, the reflection fraction is constrained to $R = 0.6^{+0.35}_{-0.2}$, while the photon index is $\Gamma = 2.17 \pm 0.05$.

Overall, a contribution of a broad disk reflection component to the iron K profile cannot be excluded, although the presence of a fast disk wind is still required in any event to account for the deep 9 keV absorption trough. In the context of disk reflection, the low emissivity index could be consistent with a more extended X-ray corona and indeed, an extended coronal component has been suggested in I Zw 1 by Wilkins et al. (2017)

---

[5] Here, the reflection fraction is defined as the ratio of the reflected flux to that of the incident power law, calculated over the 3–100 keV energy range.
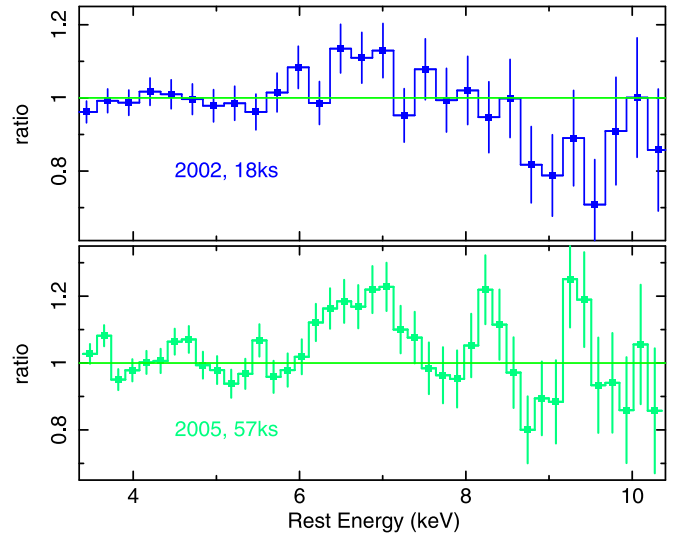
Figure 6. Data/model ratio for the 2002 (top) and 2005 (lower) spectra against a simple power-law model. The residuals in the 2002 spectrum are similar to the 2015 spectra, with a broad absorption trough near 9 keV. In contrast, the 2005 spectrum appears dominated by ionized emission, both from a broad Fe Lyα emission line near 7 keV, as well as possible higher order features near 8.3 and 9.3 keV.

based upon its X-ray timing properties. It should be noted that the wind itself can also produce significant X-ray reflection via scattering off the wind surface. This latter contribution will be investigated later in Section 5, using the physically motivated accretion disk wind models of Sim et al. (2008, 2010). These self-consistently compute both the line-of-sight absorption from the wind and the scattered wind emission integrated over all angles and accounting for relativistic effects.

4.4. Wind Variability

The earlier *XMM-Newton* data sets of I Zw 1 were also compared to the above XSTAR model to place any additional constraints on the possible wind, as well as any long-term variability. These 2002 and 2005 data sets were originally analyzed by Gallo et al. (2004) and Porquet et al. (2004) for the 2002 observation, and by Gallo et al. (2007) for the 2005 observation, and in all of these analyses, a broad ionized iron K emission line was found. We re-extracted these EPIC-pn spectra from these observations as per Section 2, yielding net exposures of 18 ks and 57 ks for 2002 and 2005, respectively (see Table 1), shorter than the 2015 observations. The background level was low in both of these observations. As per the 2015 observations, the spectra were binned into constant-energy intervals and with a minimum signal-to-noise ratio of 5, which resulted in the short 18 ks spectrum having a coarser binning of $\Delta E = 240$ eV per bin.

The ratio of these spectra to a simple power-law model (absorbed only by the neutral Galactic absorber) is shown in Figure 6. Although it is of lower signal to noise, the 2002 spectrum displays residuals similar to the two 2015 observations, with an excess of emission due to ionized iron around 7 keV and a broad absorption trough centered near 9 keV. Application of the XSTAR model in Section 4.2, with a 25,000 km s^{-1} velocity broadening, yielded a very good fit to the 2002 spectrum. The best-fit column density of $N_H = 4.8^{+2.3}_{-2.0} \times 10^{23}$ cm^{-2} and outflow velocity of $v/c = -0.29 \pm 0.03$ were consistent with the 2015 spectra, and

overall, the addition of the fast absorber improved the fit statistic by $\Delta\chi^2 = 17$ for $\Delta\nu = 2$. The only apparent difference with the 2015 observations is the continuum flux, which was about 50% higher in 2002 (see Table 3 for details). Note that the ionization parameter was fixed at $\log\xi = 4.9$, per the 2015 spectra, as otherwise it was poorly constrained due to the short exposure.

In contrast, the residuals of the 2005 spectrum to a power-law continuum appear quite different from those of the other spectra. While broad ionized emission is present near 7 keV, emission-like residuals also appear to be present at higher energies, notably at 8.3 keV and 9.3 keV in the AGN rest frame, while no strong absorption trough is present. Overall, the fit to a simple power-law model resulted in a very poor fit to the 2005 spectrum, with $\chi^2_\nu = 81.5/41 = 1.99$, rejected at >99.99% confidence. The 2–10 keV flux is similar to the 2015 observations. Most of the contribution toward χ^2 arises from the broad Fe Kα component near 7 keV ($\Delta\chi^2 = 35$ for $\Delta\nu = 3$ when fitted with a Gaussian), while the higher energy features are more marginal (with $\Delta\chi^2 = 7$ and $\Delta\chi^2 = 6$ for the 8.3 and 9.3 keV features, respectively). However, despite their low significance, the rest-frame energies of the high-energy features are entirely consistent with the expected emission from the higher order Fe XXVI Lyβ line and the respective radiative recombination continuum feature from H-like iron.

The 2005 spectrum was first fitted with the 25,000 km s^{-1} XSTAR grid, in order to model the emission features. However, the velocity broadening was too large to account for the residuals. As a result, we generated another grid of photo-ionized spectral models within XSTAR, but with a lower velocity broadening of 10,000 km s^{-1}. Given that this spectrum appears more dominated by the emission, we uncoupled the emitter column from that of the absorber. For the emitter, we fixed the normalization of the XSTAR component such that it corresponds to full covering with $f = 1$, but allowed the emitter column to vary. The ionizations of the emitter and absorber were tied, as per the above analysis. Application of this model to the 2005 spectrum resulted in an acceptable fit, with $\chi^2_\nu = 44.7/37$ and was able to account for the Fe K emission features. The gas ionization is high, with $\log\xi = 5.0^{+0.5}_{-0.4}$, consistent with most of the emission arising from H-like iron as noted above, while the emitter column was found to be $N_H = 4.6^{+1.7}_{-1.3} \times 10^{23}$ cm^{-2}. The flux of the emission component (see Table 3) is similar to that observed in 2015, which suggests it may be more apparent against the continuum in 2005, which is less absorbed. Indeed, the column density of any absorption was found to be about a factor of 2–3 lower (with $N_H = 2.0^{+1.2}_{-1.1} \times 10^{23}$ cm^{-2}) compared to 2015. Thus, overall, three out of the four I Zw 1 spectra, from the 2002 and 2015 epochs, show evidence for a blueshifted iron K absorption trough, while the 2005 spectrum is dominated by the ionized iron K emission.

4.4.1. Short-term Variability

I Zw 1 shows substantial short-timescale X-ray variability within the longer 2015 observations (Wilkins et al. 2017), and thus we investigated whether there were any changes in the wind properties in response to the continuum variations. Due to the mosaic mode used, the two observations were split into 2×5 sequences, each corresponding to a different telescope pointing. While the individual sequences were too short
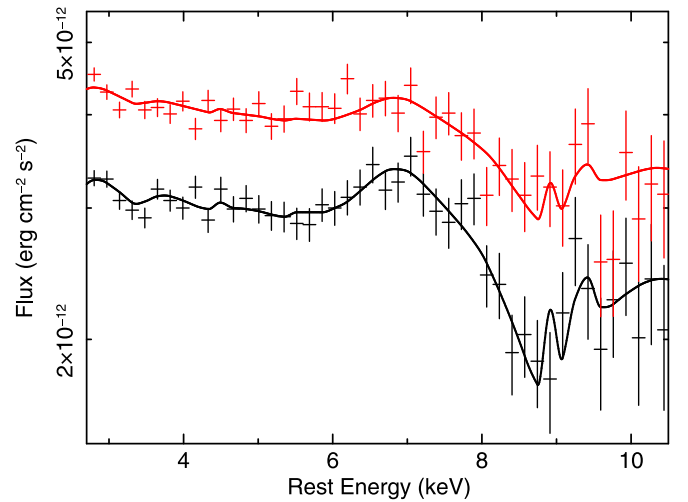
Figure 7. High (red) and low (black) flux spectra extracted from the 2015 observations. The best-fit XSTAR model is overlaid, which shows that the absorption trough is deeper in the low flux spectrum and can be accounted for by a factor of 2 change in column density. Alternatively, the change in opacity can also be modeled by variations in ionization (for a constant column), with the ionization increasing with X-ray flux. Overall, the observations are consistent with the equivalent width of the features decreasing with increasing flux, as is also seen in the NLS1 IRAS 13224−3809 (Parker et al. 2017).

($\sim$15–20 ks net exposure) to investigate the wind variability between each pointing, we did attempt to extract flux-selected spectra from a combination of these pointings. To do this, the 10 sequences across OBS 1 and OBS 2 were sorted by their 2–10 keV flux and the three brightest (or faintest) spectra were combined to create a high (or low) flux-selected spectrum. For the high flux spectrum, these consisted of the first, fourth, and fifth observations from OBS 2, while the low flux spectrum consisted of the third, fourth, and fifth spectra, all from OBS 1. The net exposures and 2–10 keV fluxes of the high and low spectra are 52.1 ks versus 54.3 ks and 6.4×10^{-12} erg cm^{-2} s^{-1} versus 4.7×10^{-12} erg cm^{-2} s^{-1}, respectively.

The high versus low flux spectra are shown in Figure 7. While the spectral shape and profile remain consistent between the spectra, the features appear weaker in the high flux spectrum. To quantify these differences, the spectra were modeled with the above XSTAR model, accounting for any changes by allowing the column density of the wind to vary, as well as the normalization of the power-law continuum, while the wind ionization was assumed to remain constant (where $\log\xi = 4.90^{+0.12}_{-0.08}$). In this case, the column density in the high flux spectrum was found to be significantly lower, with $N_H = 4.1^{+1.5}_{-1.3} \times 10^{23}$ cm^{-2} compared to the low flux case with $N_H = 8.1^{+2.0}_{-1.6} \times 10^{23}$ cm^{-2}. Alternatively, the opacity change can also be parameterized by an increase in ionization with increasing flux, where $\log\xi = 4.88^{+0.17}_{-0.13}$ for the high flux spectrum and $\log\xi = 4.58^{+0.13}_{-0.12}$ for the low flux spectrum. In this scenario, the column was assumed to remain constant with $N_H = 3.9^{+1.4}_{-1.2} \times 10^{23}$ cm^{-2}.

Thus, on short timescales, the opacity of the wind appears to be anticorrelated with the X-ray flux. Such an effect was observed in the highly variable NLS1, IRAS 13224−3809 (Parker et al. 2017; Pinto et al. 2018), where the equivalent width of the fast iron K absorption line as well as the soft X-ray absorption features appeared to diminish with increasing flux. In I Zw 1, these changes are less drastic, as the dynamic range in 2–10 keV flux is much smaller than in IRAS 13224−3809.

The opacity change here could either be due to a response in the ionization of the wind to the continuum or via modest column density variations along the wind. In the longer term, the behavior of the 2005 spectrum compared to 2015 appears very different. In the former, despite the relatively low X-ray flux, the wind absorption is much weaker. However, as was recently suggested by Gallo et al. (2019) for Mrk 335, the triggering of wind events could be related to coronal (ejection?) activity, which may lead to the onset of wind features during strong X-ray flares. A similar behavior was observed in PDS 456, during a long 2013 *Suzaku* observation (covering a 1.5 Ms baseline). There, the wind features emerged only following a major X-ray flare (Gofford et al. 2014; Matzeu et al. 2017) and preflare; despite the relatively low X-ray flux, no Fe K absorption was present. Further, more intensive monitoring on I Zw 1 would be required in order to fully understand the wind variability and how it may be related to the continuum variability.
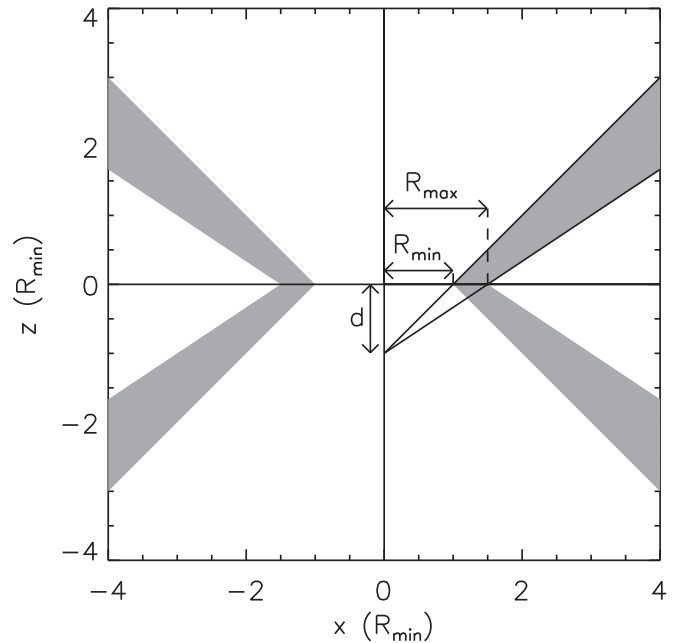
5. Disk Wind Modeling

In order to self-consistently model the wind signatures in the I Zw 1 spectra, we utilized the radiative transfer disk wind code developed by Sim et al. (2008, 2010). This model creates tables of synthetic wind spectra computed for parameterized models of smooth, steady-state 3D biconical winds, adopting the Monte Carlo ray-tracing methods described by Lucy (2002, 2003). The computed spectra contain both the radiation transmitted through the wind and reflected or scattered emission from the wind, including the iron Kα emission. The disk wind model thus provides a self-consistent treatment of both the emission and absorption arising from the wind, with a physically realistic geometry, as well as computing the (nonuniform) ionization structure and velocity field through the flow. The model incorporates extensive atomic data, covering a wide range in ionization; e.g., ions from Fe X–XXVI are included as well as those from lighter elements.

The Sim et al. (2008) wind model has been previously employed to fit the X-ray absorption absorption profiles in several AGNs, e.g., Mrk 766 (Sim et al. 2008), PG 1211 + 143 (Sim et al. 2010), and PDS 456 (Reeves et al. 2014), as well as the iron Kα emission line profiles of several AGNs (Tatum et al. 2012). Another disk wind model, similar in geometry to the Sim et al. (2008) model, but simplified by using only He- and H-like ions, was later employed by Hagino et al. (2015), who reproduced the Fe K absorption profiles in AGNs such as PDS 456, as well as in 1H 0707–495 and APM 08279+5255 (Hagino et al. 2016, 2017). Magnetohydrodynamical models have also been able to successfully model the spectra from fast outflows such as in the AGN PG 1211+143 (Fukumura et al. 2015), as well as slower winds in Galactic black hole sources, such as in GRO J1655–40 (Fukumura et al. 2017).

5.1. The Disk Wind Parameters

The inner wind geometry is illustrated in Figure 8 and is determined by the parameters below, which are not allowed to vary in any of the models. A more detailed description of the model setup can be found in Sim et al. (2008).

1. Launch radius. $R_{\rm min}$ and $R_{\rm max}$ are the inner and outermost launching radii of the wind off the disk surface, which also determines the overall thickness of the wind streamline. In the model for I Zw 1, we adopted an inner

Figure 8. Schematic of the inner disk wind model geometry. The *x*-axis represents the plane of the disk and the *z*-axis in the polar direction, in units of $R_{\rm min}$, the minimum launch radius of the flow. The black hole is at the origin, and the inclination angle is measured with respect to the *z*-axis. The shaded area represents the physical extent of the outflow. The models presented here have a minimum launch radius $R_{\rm min} = 32 R_{\rm g}$ along the disk plane. In this example, the maximum launch radius off the disk is $R_{\rm max} = 1.5 R_{\rm min}$; this parameter sets the geometric thickness of the flow. *d* is the distance of the focus point of the wind below the origin in units of $R_{\rm min}$ (here $d = 1$), as indicated by the solid lines. Increasing *d* makes the wind more polar and more collimated.

launch radius of $32 R_{\rm g}$ (where $R_{\rm g}$ is the gravitational radius), while we set $R_{\rm max} = 1.5 R_{\rm min}$ for the wind thickness. The inner wind radius was chosen as this corresponds to the escape radius for a wind of $v_\infty = 0.25c$.

2. Geometry. The wind collimation and opening angle are set by the geometrical parameter *d* (see Figure 8), which also determines how equatorial (or polar) the wind is. Here, *d* is defined as the distance of the focus point of the wind below the origin in units of $R_{\rm min}$. In the models below, a value of $d = 1$ was adopted, which at large radii ($R \gg R_{\rm min}$) corresponds to the wind having an opening angle of $\theta = \pm 45°$ with respect to the polar (*z*) axis.

In addition, the outer boundary of the disk wind simulations were set to an outer radius of $\log(R_{\rm out}/R_{\rm g}) = 4.5$, or $\sim 3.2 \times 10^4 R_{\rm g}$ ($1000 R_{\rm min}$). The X-ray source is assumed to originate from a region of radius $6 R_{\rm g}$ and is centered at the origin. Special relativistic effects are accounted for in the models.

Having set up the geometric conditions of the flow, several parameters then determine the properties of the output spectra, which are described below.

1. Terminal velocity. The terminal velocities (v_∞) realized in the wind models are determined by the choice of the inner wind radius ($R_{\rm min}$) and the terminal velocity parameter $f_{\rm v}$, which relates the terminal velocity on a wind streamline to the escape velocity at its base, via $v_\infty = f_{\rm v} \sqrt{2 G M_{\rm BH} / R}$. The terminal velocity is adjusted by varying the $f_{\rm v}$ parameter, for a given launch radius (here $R_{\rm min} = 32 R_{\rm g}$). For I Zw 1, output models were generated

for seven velocity values, ranging from $f_v = 0.5-2.0$, corresponding to terminal velocities of $0.125c - 0.50c$.

2. Input Continuum. This was set to be a power law, covering the likely range for I Zw 1 from $\Gamma = 2.0-2.4$, over $n = 3$ increments. Note that the spectra are calculated over the 0.1–500 keV range.

3. Inclination angle. The observer's inclination toward the wind is defined as $\mu = \cos\theta$, where $0.025 < \mu < 0.975$ over 20 incremental values (with $\Delta\mu = 0.05$). Here, θ is the angle between the observer's line of sight and the polar z-axis of the wind, with the disk lying in the xy plane; see Figure 8. Note that for $\mu > 0.7$ (i.e., $\theta < 45°$), the observer's line of sight does not intercept the wind; however, the output spectra contain a contribution from X-ray reflection, via photons scattered off the wind. For $\mu < 0.7$, the line of sight intercepts the wind, imprinting blueshifted absorption features, while the output spectra also contain a contribution from scattered photons in emission.

4. Mass outflow rate. This is defined by the ratio $\dot{M} = \dot{M}_{out}/\dot{M}_{Edd}$, where the mass outflow rate is normalized to the Eddington value. As a result, this parameter, as well as the luminosity below, are invariant upon the black hole mass. The grid of models here was generated covering the range $\dot{M} = 0.02-0.68$, in $n = 12$ increments, with equal logarithmic spacing. Higher values of $\dot{M}$ result in spectra with stronger emission and absorption features.

5. Ionizing X-ray luminosity. The X-ray luminosity is parameterized in the 2–10 keV band as a percentage of the Eddington luminosity, where $L_X = L_{2-10\,keV}/L_{Edd}$. The luminosity parameter sets the overall ionization of the wind, and lower L_X values result in the wind being less ionized and more opaque to X-rays. Here, the spectral models were generated over the range of L_X of 0.025% to 0.8% of the Eddington luminosity, over $n = 7$ increments in equal logarithmic spacing. These relatively low L_X values ensure the wind is not overly ionized so as to produce a featureless output spectrum.

The result of the above simulations is a grid of models with $7 \times 3 \times 20 \times 12 \times 7 = 35,280$ synthetic spectra, covering the above parameter space in f_v, Γ, μ, $\dot{M}$, and L_X. The spectra are tabulated into FITS format files and are used as multiplicative grids within XSPEC. Note that in the fitting procedure, interpolation is used to determine the best-fit parameter values and their errors if these fall in between grid points.

5.2. Disk Wind Results

The above disk wind model was then applied to the two 2015 pn spectra of I Zw 1. The form of the model is simply TBABS × DISKWIND × POWERLAW. Note that the input photon index of the DISKWIND model is tied to the direct power-law continuum. The OBS 1 and OBS 2 spectra were fitted simultaneously as above, while all the diskwind parameters, except for the ionizing luminosity, were tied between the data sets. The power-law normalizations were allowed to vary independently. The results of the diskwind fits are summarized in Table 4 and produced a good fit to the data, with a fit statistic of $\chi^2_\nu = 83.7/82$. An inclination angle of $\sim 50°$ ($\mu = 0.65 \pm 0.02$) was required, implying that the sightline directly intercepts the innermost fastest wind
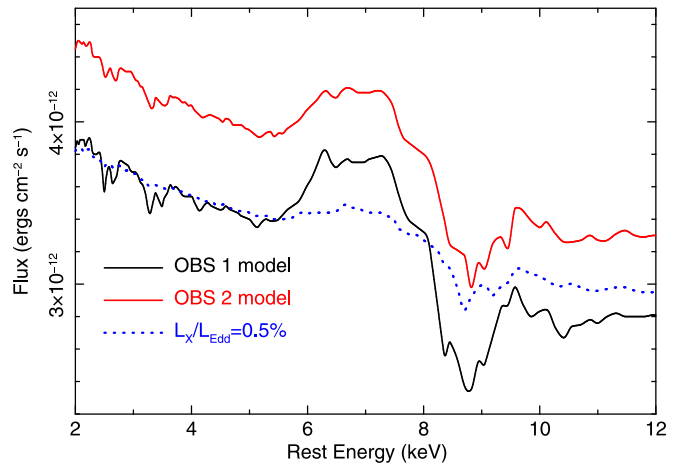
Figure 9. Model spectra generated with the disk wind radiative transfer code of Sim et al. (2008). The solid black and red lines correspond to the best-fitting models to the OBS 1 and OBS 2 spectra, which have a mass outflow rate of 20% of Eddington (see Table 4 for details). The model can reproduce the Fe K profile, with a terminal velocity of $v/c = -0.28 \pm 0.01$. The dashed blue curve shows the effect upon the model when the incident 2–10 keV luminosity is increased from 0.14% to 0.5% of Eddington for OBS 1. As a result, the profile is much weaker as the gas becomes more ionized and subsequently fails to account for the Fe K profile.

Table 4
Disk Wind Model Results

Parameter	OBS 1	OBS 2
$\dot{M}_{out}/\dot{M}_{Edd}$ [a]	$0.19^{+0.16}_{-0.08}$	0.19 [e]
% L_{2-10}/L_{Edd} [b]	$0.14^{+0.16}_{-0.07}$	$0.22^{+0.24}_{-0.11}$
v_∞/c	-0.280 ± 0.010	-0.28 [e]
$\mu = \cos\theta$ [c]	0.647 ± 0.015	0.647 [e]
Γ	2.16 ± 0.03	2.16 [f]
$L_{2-10\,keV}$ [d]	5.5	6.3

Notes.
[a] Mass outflow rate in Eddington units.
[b] Percentage of ionizing (2–10 keV) luminosity to Eddington luminosity.
[c] Cosine of wind inclination, with respect to the polar axis.
[d] Intrinsic 2–10 keV luminosity, in units of 10^{43} erg s^{-1}.
[e] Denotes parameter is tied between observations.
[f] Parameter is fixed.

streamline. The terminal velocity is similar to what was found previously, with $v_\infty = -0.28 \pm 0.01c$ (corresponding to $f_v = 1.11 \pm 0.04$).

Figure 9 shows the output spectra for the best-fit models fitted to OBS 1 and OBS 2, which reproduces both the Fe K emission and absorption well. The best-fit mass outflow rate for these spectra (tied between the two observations) is $\dot{M} = \dot{M}_{out}/\dot{M}_{Edd} = 0.19^{+0.16}_{-0.08}$, i.e., about 20% of Eddington. The ionizing X-ray luminosity is $L_X = 0.14^{+0.16}_{-0.07}\%$ for OBS 1 and is only marginally higher for OBS 2, with $L_X = 0.22^{+0.24}_{-0.11}\%$. Overall, the model prefers a solution whereby the incident 2–10 keV luminosity is about 0.2% of the Eddington value. In comparison, the observed 2–10 keV luminosity is about 6×10^{43} erg s^{-1}, closer to 2% of the Eddington luminosity, i.e., an order of magnitude higher than predicted by the model. This may suggest that the wind is underionized compared to what one would predict from the observed X-ray luminosity. Indeed, in Figure 9 we also plot the predicted profile if the X-ray luminosity is increased in OBS 1 to 0.5% of
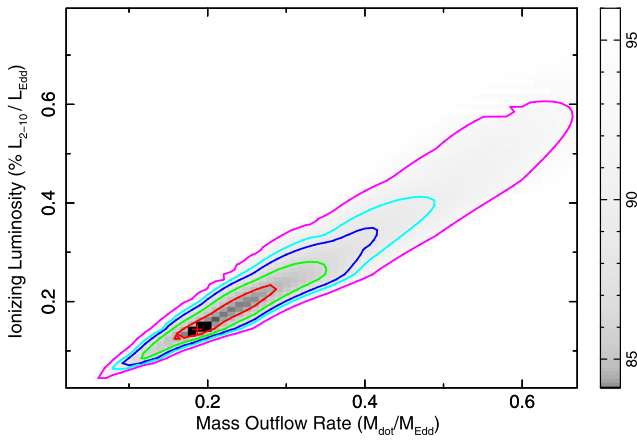
Figure 10. Confidence contours for the ionizing luminosity vs. mass outflow rate for the wind model, where the contours represent the 68%, 90%, 95%, 99%, and 99.9% significance levels for two interesting parameters. The color bar shows the χ^2 space in gray scale, where darker regions have lower χ^2 values; note that the best fit is $\chi^2_\nu = 83.7/82$. The mass outflow rate is constrained between 11%–35% of Eddington at 90% confidence, while the ionizing 2–10 keV X-ray luminosity is lower than the expected 2% of Eddington value, which suggests the wind is underionized.

Eddington (blue dotted curve); this increases the wind ionization, resulting in a much shallower profile than is observed in the data, with much weaker emission and absorption.

To investigate this, we ran confidence contours between $\dot{M}$ and L_X to explore the full model parameter space and allowing the other wind parameters to vary at each grid point. Figure 10 shows the contours for OBS 1, at the 68%, 90%, 95%, 99%, and 99.9% confidence levels for two parameters of interest. This confirms that the mass outflow rate is constrained between 11% and 35% of Eddington at the 90% level. The direction of the contours shows that as the X-ray luminosity increases, the mass outflow rate also increases to try to compensate (by increasing the column density along the flow). However, higher luminosities can still be ruled out; e.g., the 99% upper limit is $L_X < 0.4\%$, as the flow becomes too highly ionized to reproduce the strong Fe K profile. This discrepancy between the ionizing versus observed luminosity could arise if the outflow is at least partially shielded from the X-ray continuum source, or if the hard X-ray continuum above 10 keV is steeper than expected. It may also be the case that the wind is inhomogeneous and clumpy, as opposed to the smooth wind model investigated here. Indeed, by involving a moderate microclumping factor of ~0.01, Matthews et al. (2016) can account for some of the UV line profiles in BAL QSOs, without requiring the intrinsic X-ray luminosity to be suppressed.

6. Discussion

6.1. Kinematics of the X-Ray Wind

Here we compute the energetics of the fast X-ray wind for the three different wind models, comparing both the XSTAR and P Cygni cases with the diskwind model above. Following the methodology of Nardini et al. (2015), we adopt the mass outflow rate in the form

$$\dot{M}_{\rm out} = \Omega \mu m_{\rm p} N_{\rm H} R_{\rm in} v, \qquad (5)$$

where Ω is the overall wind solid angle, $\mu m_{\rm p}$ is the mean baryonic mass per particle ($\mu \sim 1.3$ for solar abundances), $N_{\rm H}$

Table 5
Derived Outflow Energetics for I Zw 1

	xstar	Diskwind	P Cygni	CO
$\dot{M}^{\rm a}$	0.15 ± 0.04	$0.19^{+0.16}_{-0.08}$	0.25 ± 0.05	$\cdots$
	(0.09 ± 0.04)	$(0.11^{+0.15}_{-0.06})$	(0.15 ± 0.06)	(<140)
$\dot{E}^{\rm b}$	0.054 ± 0.013	$0.08^{+0.07}_{-0.03}$	0.15 ± 0.04	$<3 \times 10^{-3}$
	(2×10^{44})	(3×10^{44})	(5×10^{44})	$(<1 \times 10^{43})$
$\dot{p}^{\rm c}$	0.4 ± 0.1	$0.5^{+0.4}_{-0.2}$	0.9 ± 0.2	<4

Notes.
[a] Mass outflow rate in Eddington units. Note absolute values are given in parentheses in units of solar masses per year.
[b] Outflow kinetic power in Eddington units. Absolute values are given in parentheses in units of erg s^{-1}.
[c] Outflow momentum rate in Eddington units.

is the hydrogen column density, v is the wind (terminal) velocity, and $R_{\rm in}$ is the inner launch radius of wind. For the XSTAR model, we adopt $\Omega/4\pi = 0.5$ (consistent with the ratio between the absorbed versus emitted flux), while the P Cygni model (spherical wind) implicitly assumes $\Omega/4\pi = 1$. For the column density, for the XSTAR model we calculated the mean value over the four observations in Table 3, of $N_{\rm H} = 4.7 \pm 1.1 \times 10^{23}$ cm^{-2}, while for the P Cygni model, we took the average of the two 2015 observations in Section 3.2, of $N_{\rm H} = 5.0 \pm 0.9 \times 10^{23}$ cm^{-2}.

The wind launch radius was set to the escape radius from the black hole, i.e., $R_{\rm in} = 2GM_{\rm BH}/v^2$, which gives the smallest inner radius of the wind and thus a more conservative estimate of the mass outflow rate. The mass outflow rate, normalized to the Eddington rate where $\dot{M}_{\rm Edd} = 4\pi GM_{\rm BH}m_{\rm p}/\sigma_{\rm T}\eta c$, is then

$$\dot{M} = \frac{\dot{M}_{\rm out}}{\dot{M}_{\rm Edd}} = 2\frac{\Omega}{4\pi}\mu N_{\rm H}\sigma_{\rm T}\eta\left(\frac{v}{c}\right)^{-1}, \qquad (6)$$

where we adopt $\eta = 0.1$ for the accretion efficiency and $\sigma_{\rm T}$ is the Thomson cross section. Subsequently the wind kinetic power, $L_{\rm k}$, normalized to the Eddington luminosity, is

$$\dot{E} = \frac{L_{\rm k}}{L_{\rm Edd}} = \frac{1}{2\eta}\frac{\dot{M}_{\rm out}}{\dot{M}_{\rm Edd}}\left(\frac{v}{c}\right)^2 = \frac{\Omega}{4\pi}\mu N_{\rm H}\sigma_{\rm T}\frac{v}{c}. \qquad (7)$$

The wind momentum rate (thrust) of the wind is $\dot{p}_{\rm out} = \dot{M}_{\rm out}v$, while that of the radiation field is $\dot{p}_{\rm Edd} = L_{\rm Edd}/c$ (where for I Zw 1 $L_{\rm bol} \sim L_{\rm Edd}$). Thus,

$$\dot{p} = \frac{\dot{p}_{\rm out}}{\dot{p}_{\rm Edd}} = \frac{1}{\eta}\frac{\dot{M}_{\rm out}}{\dot{M}_{\rm Edd}}\frac{v}{c} = 2\mu\frac{\Omega}{4\pi}N_{\rm H}\sigma_{\rm T} \sim \tau \qquad (8)$$

and τ is the optical depth to Compton scattering. Thus, the inner wind is approximately momentum conserving against the radiation field in the single photon scattering limit, where $\tau \sim 1$ (e.g., King & Pounds 2003).

We calculated the above values of $\dot{M}$, $\dot{E}$, and $\dot{p}$ for the both the XSTAR and P Cygni models, and we used the best-fit value of $\dot{M}$ for the diskwind model to calculate the corresponding values of $\dot{E}$ and $\dot{p}$. Table 5 shows the resulting values, while we also give the absolute values of the mass outflow rate ($\dot{M}_{\rm out}$) and kinetic luminosity ($L_{\rm k}$), for a black hole mass of $M_{\rm BH} = 2.8^{+0.6}_{-0.7} \times 10^7 \; M_\odot$ and a corresponding Eddington luminosity of $L_{\rm Edd} = 3.5 \times 10^{45}$ erg s^{-1}.

Overall, the derived mass outflow rate is between 15% and 25% of Eddington, corresponding to ~0.1–0.15 $M_\odot$ yr^{-1},

while the wind kinetic power ranges between 5% and 15% of Eddington (or $L_k = (2-5) \times 10^{44}$ erg s^{-1}), which is potentially significant for mechanical feedback on larger scales (Hopkins & Elvis [2010]). These values are typical of those found in ultrafast outflows in other AGNs (Tombesi et al. [2013]; Gofford et al. [2015]). The wind momentum rate is of the order unity or just below ($\dot{p} \sim 0.4{-}0.9$), which is also in agreement with other ultrafast outflows; e.g., see Figure [4], Tombesi et al. ([2013]).

Reassuringly, the outflow rate and kinetic power obtained between the three models are consistent within the uncertainties, despite any differences in physical construction between them. Of the three models, the XSTAR model has the most complete atomic physics, but is the least self-consistent geometrically, as the absorption is computed from a one-dimensional slab, although the comparison between the total emission versus absorption does make it possible to estimate the overall covering fraction of the gas. Both the P Cygni and disk wind models have the advantage of being physically motivated wind models, where the subsequent velocity profiles (in emission and absorption) are self-consistently calculated for a given terminal velocity over all solid angles, where the former assumes a spherical wind and the latter a biconical outflow. The disk wind model has the further advantage in that the outflow parameters derived are independent of the black hole mass, as the output spectra are invariant upon this parameter for a realistic range of AGN black hole masses. Of all three models, the values for the P Cygni model lie on the upper end of the range, due to its spherical geometry and the higher terminal velocity obtained ($v_\infty = 0.35^{+0.03}_{-0.04}c$), which could be considered to be the least conservative scenario.

6.1.1. Comparison with the Wind in PDS 456

We also compare the wind properties of I Zw 1 with those obtained from the prototype disk wind quasar PDS 456. For illustration, Figure [11] shows the Fe K wind profile of I Zw 1 compared to the spectrum consisting of the third and fourth observations from the 2013–2014 *XMM-Newton* campaign on PDS 456. This is the same spectrum that was analyzed by Nardini et al. ([2015]), where a broad Fe K P-Cygni profile was first found in this QSO. The profiles of PDS 456 and I Zw 1 are remarkably similar, as both show an excess in emission above the continuum between 6 and 8 keV, while a deep broad absorption trough is present above 8 keV in both quasars. It is noticeable that the blueshift of the absorption trough is slightly larger in PDS 456, where $v/c = 0.29 \pm 0.01$ from the absorption-line centroid, although we note that the outflow velocity in PDS 456 has been observed to vary from $0.25c$ to $0.35c$ over all X-ray observations (2001–2017) to date (Matzeu et al. [2017]).

From analyzing all five *XMM-Newton* and *NuSTAR* observations of PDS 456 in 2013–2014, Nardini et al. ([2015]) obtained an average column density of $N_H = 6.9^{+0.6}_{-1.2} \times 10^{23}$ cm^{-2} for the Fe K wind, while the profile was consistent with a minimum covering of $\Omega = 2\pi$ sr. Adopting these values and setting the inner wind radius equal to the escape radius for consistency, then for PDS 456 $\dot{M} \sim 0.2$ (or $\sim 5 M_\odot$ yr^{-1}), while $\dot{E} \sim 0.1$ (or $L_k \sim 10^{46}$ erg s^{-1}) and $\dot{p} \sim 1$. In terms of their Eddington values, the outflow energetics are very similar between both I Zw 1 and PDS 456, with the higher absolute values in PDS 456 being due to its larger black hole mass of $10^9 M_\odot$. Thus, the wind in I Zw 1 may be a lower mass analog of
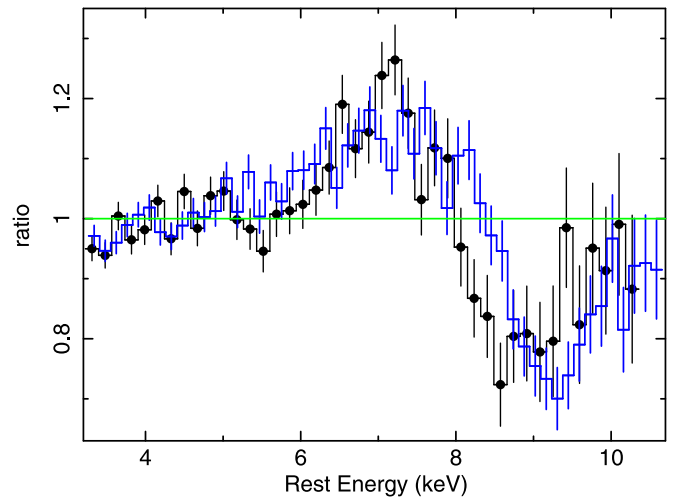

Figure 11. Comparison between the Fe K wind profiles in I Zw 1 and the quasar PDS 456. The black circles show the I Zw 1 2015 OBS 1 profile, while the blue points show the pn profile of PDS 456, from the third and fourth observations of the 2013–2014 *XMM-Newton* campaign (Nardini et al. [2015]). Both AGNs are plotted in their respective rest frames ($z = 0.184$ for PDS 456, $z = 0.0611$ for I Zw 1) and are shown as a ratio against a simple absorbed power-law continuum. The profiles show strong similarities; both require broadened emission centered near 7 keV as well as a broad, blueshifted absorption trough above 8 keV, of similar optical depth. The blueshift of the 2013 PDS 456 profile is slightly higher than in I Zw 1, suggesting a somewhat higher outflow velocity. The wind energetics are similar for both AGNs, with the mass outflow rate and kinetic power typically of 10% Eddington (see Section [6.1]). Overall, I Zw 1 may represent a lower mass analog of the powerful disk wind in PDS 456.

the one in PDS 456, where in both AGNs, the high accretion rate close to Eddington likely creates favorable conditions for driving a fast disk wind.

6.2. Comparison with the Molecular Gas Outflows

The energetics for the X-ray wind are now compared to observations of the molecular gas in I Zw 1, through the CO(1–0) line, to ascertain the mechanical effect of the wind on the large-scale star-forming ISM gas. Observations of I Zw 1 were made with the IRAM PdBI in 2010, which spatially and kinematically resolved the CO emission on about kiloparsec scales, and the results were reported in Cicone et al. ([2014]). Unlike the clear signature of outflow for the X-ray wind, the CO observations show no clear evidence of any large-scale molecular outflow. The continuum-subtracted CO emission line profile (see Cicone et al. [2014], Figure 7) is narrow with no apparent blueshift or broad wings, yielding an upper limit to its velocity width of <500 km s^{-1} (at FWZI). This is also consistent with the lack of any blueshift in either emission or absorption in I Zw 1 from the OH profiles as measured by *Herschel*-PACS (Veilleux et al. [2013]). The CO velocity map does show clear evidence of rotation, via double-peaked emission and which is likely associated with a disk of molecular gas within the host galaxy.

Cicone et al. ([2014]) subsequently derived an upper limit of $140 M_\odot$ yr^{-1} for the total molecular mass outflow rate in I Zw 1, after adopting conservative upper limits of $v < 500$ km s^{-1} from the CO profile and $r < 500$ pc from the spatial extent of the narrow core. For comparison with the X-ray wind, we then computed the upper limits to both the kinetic power and momentum rate for any molecular outflow, which are also reported in Table [1]. The upper limit to
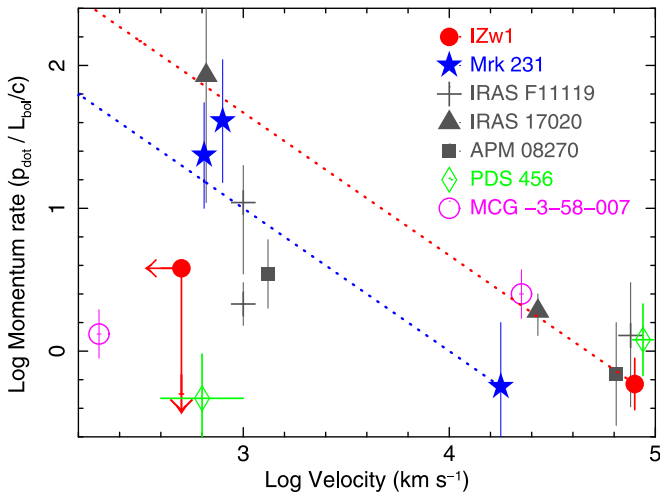
Figure 12. Comparison between momentum rates (normalized by L_{bol}/c) and outflow velocity for the six ultrafast outflows with reported measurements of molecular outflows. Data points as marked correspond to I Zw 1 (Cicone et al. 2014; this paper), Mrk 231 (Feruglio et al. 2015), IRAS F11119+3257 (Tombesi et al. 2015; Veilleux et al. 2017), IRAS 17020+4544 (Longinotti et al. 2015, 2018), APM 08279+5255 (Feruglio et al. 2017), PDS 456 (Bischetti et al. 2019), and MCG–03-58-007 (Braito et al. 2018; Sirressi et al. 2019). Note that for Mrk 231, both CO components are plotted separately, as well as the separate CO and OH measurements of IRAS F11119+3257. The dotted lines correspond to the predicted momentum load factors in I Zw 1 (red line) and Mrk 231 (blue line) for the energy-conserving scenario. The molecular wind in Mrk 231 is consistent with being energy driven, in contrast to I Zw 1, PDS 456, and MCG–03-58-007, where the momentum rate of the molecular gas lies about two orders of magnitude below the energy-conserving relation.

the kinetic power for $v < 500\ km\ s^{-1}$ is subsequently $L_K < 1 \times 10^{43}\ erg\ s^{-1}$, corresponding to $L_K/L_{Edd} < 3 \times 10^{-3}$. This is more than an order of magnitude lower than the kinetic power of the X-ray wind, which gave $L_K = (2\text{–}5) \times 10^{44}\ erg\ s^{-1}$. On the other hand, the momentum rate for the molecular gas is $\dot{p}/\dot{p}_{Edd} < 4.0$, which is consistent with the outflow being momentum rather than energy conserving on large scales.

The outflow in I Zw 1 can also be compared with other AGNs where both an ultrafast disk wind and a kiloparsec-scale molecular outflow coexist. In Figure 12, we plot the momentum rates of the X-ray versus molecular phases of the outflows against wind velocity for the five AGNs which have been reported to host both an ultrafast disk wind and a large-scale molecular outflow. The first reported examples were in the ultraluminous infrared galaxies (ULIRGs)/type II QSOs Mrk 231 (Feruglio et al. 2015) and IRAS F11119+3257 (Tombesi et al. 2015), where the detection of an energy-conserving molecular outflow implied that the kinetic power of the fast wind was effectively transferred out to larger scale gas. However, even from the small sample plotted in Figure 12, it is apparent that not all of the large-scale outflows lie on the predicted relation for an energy-driven wind. Indeed, only Mrk 231 and the NLS1 IRAS 17020+4544 (Longinotti et al. 2015, 2018) are consistent with the scenario whereby the black hole wind drives an energy-conserving molecular outflow out to large scales. In complete contrast, an energy-conserving wind can be clearly ruled out in I Zw 1, as the momentum rate for the molecular gas lies nearly two orders of magnitude below the predicted value for an energy-driven outflow. A similar scenario also applies to the high-redshift QSO APM 08279 + 5255 (Feruglio et al. 2017), where the measured momentum boost is lower than the prediction for an energy-conserving

wind. Even the original case of IRAS F11119+3257 now appears more complex, as recent ALMA CO measurements (Veilleux et al. 2017) suggest that the momentum boost is lower than that originally derived from the *Herschel* OH profile in Tombesi et al. (2015) and which was also further noted by Nardini & Zubovas (2018).

These results suggest a range of efficiencies in transferring the kinetic energy of the inner wind out to the large-scale molecular component. This is consistent with the recent analysis of Mizumoto et al. (2019), who analyzed a small X-ray sample of eight AGNs (including I Zw 1), selected from the Cicone et al. (2014) CO sample. Mizumoto et al. (2019) inferred that the energy transfer rate, from the black hole wind to the molecular gas, spanned a wide range of efficiency from $\epsilon \sim 7 \times 10^{-3} - 1$ (where $\epsilon = 1$ corresponds to a perfectly energy-conserving outflow). Similarly, the AGN outflows compiled by Fiore et al. (2017) show a wide range of momentum load factors, with about half of the AGNs receiving a boost of at least $\times 10$ in the molecular outflow component compared to the X-ray wind.

We also caution that comparing the energetics of the nuclear and larger scale outflows is challenging, especially when the host is a powerful ULIRG, which are generally characterized by a high star formation rate. In these objects, powerful galactic-scale outflows are common and could involve different gas phases (Cicone et al. 2018). Nonetheless, the energetics of the molecular outflows seen in Mrk 231 and IRAS 17020 +4544 (where $L_k > 10^{44}\ erg\ s^{-1}$) are too large to be solely explained by the star formation activity. The large momentum boost $(\dot{p}_{CO}/\dot{p}_X > 10)$ measured for both these outflows suggests that the mechanical energy of the inner AGN disk wind is efficiently carried to the large-scale outflows.

In I Zw 1, like in PDS 456, the AGN emission dominates with respect to the star-forming activity. Interestingly, from very recent ALMA observations, Bischetti et al. (2019) for the first time resolved the large-scale molecular outflow in CO from PDS 456. These observations revealed a complex and clumpy outflow, extending up to 5 kpc from the nucleus. The total molecular mass outflow rate measured in PDS 456 is 180–760 $M_{\odot}\ yr^{-1}$, with a corresponding momentum rate of $(7.8\text{–}32) \times 10^{35}$ dyne. Compared to the bolometric luminosity of PDS 456 of $10^{47}\ erg\ s^{-1}$, $\dot{p}_{CO}/\dot{p}_{rad} \lesssim 1$; this is clearly consistent with a momentum- rather than energy-conserving outflow. Indeed, the very sensitive ALMA observations are very stringent in PDS 456 and place the quasar in the same region of the momentum rate versus velocity diagram as I Zw 1 (see Figure 12). Bischetti et al. (2019) suggest that part of the large-scale outflow in PDS 456 could plausibly be in the form of ionized instead of molecular gas, thereby leading to the total mass outflow rate being underestimated. Alternatively, the conditions for a large-scale energy-conserving outflow (Zubovas & King 2012) could break down in such a luminous quasar.

Another powerful disk wind was recently discovered in the nearby ($z = 0.031462$), luminous Seyfert 2 galaxy, MCG–03-58-007 (Braito et al. 2018; Matzeu et al. 2019). This AGN appears similar to both I Zw 1 and PDS 456 in its X-ray characteristics, while the AGN has a similar bolometric luminosity to I Zw 1 of $L_{bol} \sim 3 \times 10^{45}\ erg\ s^{-1}$. In this object, the disk wind has a kinetic power of $\sim 10\%$ of L_{bol}, while its host galaxy has only a modest star formation rate ($\sim 10 M_{\odot}\ yr^{-1}$; Oi et al. 2010). The subsequent analysis of a recent ALMA observation of this AGN (Sirressi et al. 2019) shows

that it hosts a rather weak kiloparsec-scale outflow in CO, consistent with a momentum-driven wind with $\dot{p}_{CO}/\dot{p}_X \sim 1$ and where the energy efficiency factor between the molecular and X-ray wind is remarkably low ($\epsilon < 10^{-3}$), similar to both PDS 456 and I Zw 1. Further CO measurements of AGNs with fast X-ray winds (and vice versa) are now clearly required to establish how efficient or not the black hole winds are at transferring their mechanical energy out to gas at kiloparsec scales and thus their overall role in large-scale feedback.

ORCID iDs

J. N. Reeves ⬤ https://orcid.org/0000-0003-3221-6765
V. Braito ⬤ https://orcid.org/0000-0002-2629-4989

References

Behar, E., Kaspi, S., Reeves, J., et al. 2010, ApJ, 712, 26
Bianchi, S., Guainazzi, M., Matt, G., & Fonseca Bonilla, N. 2007, A&A, 467, L19
Bischetti, M., Piconcelli, E., Feruglio, C., et al. 2019, A&A, 628, A118
Boller, T., Brandt, W. N., & Fink, H. 1996, A&A, 305, 53
Braito, V., Reeves, J. N., Matzeu, G. A., et al. 2018, MNRAS, 479, 3592
Brightman, M., & Nandra, K. 2011, MNRAS, 413, 1206
Chartas, G., Brandt, W. N., Gallagher, S. C., & Garmire, G. P. 2002, ApJ, 579, 169
Chartas, G., Saez, C., Brandt, W. N., Giustini, M., & Garmire, G. P. 2009, ApJ, 706, 644
Cicone, C., Brusa, M., Ramos Almeida, C., et al. 2018, NatAs, 2, 176
Cicone, C., Maiolino, R., Gallerani, S., et al. 2015, A&A, 574, A14
Cicone, C., Maiolino, R., Sturm, E., et al. 2014, A&A, 562, A21
Costantini, E., Gallo, L. C., Brandt, W. N., Fabian, A. C., & Boller, T. 2007, MNRAS, 378, 873
Di Matteo, T., Springel, V., & Hernquist, L. 2005, Natur, 433, 604
Done, C., Sobolewska, M. A., Gierliński, M., & Schurch, N. J. 2007, MNRAS, 374, L15
Fabian, A. C. 1999, MNRAS, 308, L39
Faucher-Giguère, C.-A., & Quataert, E. 2012, MNRAS, 425, 605
Ferrarese, L., & Merritt, D. 2000, ApJ, 539, 9
Feruglio, C., Ferrara, A., Bischetti, M., et al. 2017, A&A, 608, A30
Feruglio, C., Fiore, F., Carniani, S., et al. 2015, A&A, 583, 99
Feruglio, C., Maiolino, R., Piconcelli, E., et al. 2010, A&A, 518, L155
Fiore, F., Feruglio, C., Shankar, F., et al. 2017, A&A, 601, A143
Fukumura, K., Kazanas, D., Contopoulos, I., & Behar, E. 2010, ApJL, 723, L228
Fukumura, K., Kazanas, D., Shrader, C., et al. 2017, NatAs, 1, 0062
Fukumura, K., Tombesi, F., Kazanas, D., et al. 2015, ApJ, 805, 17
Gallo, L. C., Boller, T., Brandt, W. N., Fabian, A. C., & Vaughan, S. 2004, A&A, 417, 29
Gallo, L. C., Brandt, W. N., Costantini, E., et al. 2007, MNRAS, 377, 391
Gallo, L. C., Gonzalez, A. G., Waddell, S. G. H., et al. 2019, MNRAS, 484, 4287
García, J., Dauser, T., Reynolds, C. S., et al. 2013, ApJ, 768, 146
Gebhardt, K. 2000, ApJ, 539, 13
Gofford, J., Reeves, J. N., Braito, V., et al. 2014, ApJ, 784, 77
Gofford, J., Reeves, J. N., McLaughlin, D. E., et al. 2015, MNRAS, 451, 4169
Gofford, J., Reeves, J. N., Tombesi, F., et al. 2013, MNRAS, 430, 60
Grevesse, N., & Sauval, A. J. 1998, SSRv, 85, 161
Hagino, K., Done, C., Odaka, H., Watanabe, S., & Takahashi, T. 2017, MNRAS, 468, 1442
Hagino, K., Odaka, H., Done, C., et al. 2015, MNRAS, 446, 663
Hagino, K., Odaka, H., Done, C., et al. 2016, MNRAS, 461, 3954
Hamann, F., Chartas, G., Reeves, J., & Nardini, E. 2018, MNRAS, 476, 943
Hopkins, P. F., & Elvis, M. 2010, MNRAS, 401, 7
Ikeda, S., Awaki, H., & Terashima, Y. 2009, ApJ, 692, 608
Iwasawa, K., & Taniguchi, Y. 1993, ApJL, 413, L15
Kalberla, P. M. W., Burton, W. B., Hartmann, D., et al. 2005, A&A, 440, 775
Kallman, T. R., Palmeri, P., Bautista, M. A., Mendoza, C., & Krolik, J. H. 2004, ApJS, 155, 675
King, A., & Pounds, K. 2015, ARA&A, 53, 115
King, A. R. 2003, ApJL, 596, L27
King, A. R. 2010, MNRAS, 402, 1516
King, A. R., & Pounds, K. A. 2003, MNRAS, 345, 657
Kosec, P., Buisson, D. J. K., Parker, M. L., et al. 2018, MNRAS, 481, 947
Leighly, K. M. 1999, ApJS, 125, 317
Longinotti, A. L., Krongold, Y., Guainazzi, M., et al. 2015, ApJL, 813, L39
Longinotti, A. L., Vega, O., Krongold, Y., et al. 2018, ApJL, 867, L11
Lucy, L. B. 2002, A&A, 384, 725
Lucy, L. B. 2003, A&A, 403, 261
Maiolino, R., Gallerani, S., Neri, R., et al. 2012, MNRAS, 425, L66
Matthews, J. H., Knigge, C., Long, K. S., et al. 2016, MNRAS, 458, 293
Matzeu, G. A., Braito, V., Reeves, J. N., et al. 2019, MNRAS, 483, 2836
Matzeu, G. A., Reeves, J. N., Braito, V., et al. 2017, MNRAS, 472, L15
Matzeu, G. A., Reeves, J. N., Nardini, E., et al. 2018, MNRAS, 458, 1311
Mizumoto, M., Izumi, T., & Kohno, K. 2019, ApJ, 871, 156
Murphy, K. D., & Yaqoob, T. 2009, MNRAS, 397, 1549
Nandra, K., George, I. M., Mushotzky, R. F., Turner, T. J., & Yaqoob, T. 1997, ApJL, 488, L91
Nandra, K., O'Neill, P. M., George, I. M., & Reeves, J. N. 2007, MNRAS, 382, 194
Nardini, E., Reeves, J. N., Gofford, J., et al. 2015, Sci, 347, 860
Nardini, E., & Zubovas, K. 2018, MNRAS, 478, 2274
Oi, N., Imanishi, M., & Imase, K. 2010, PASJ, 62, 1509
Osterbrock, D. E., & Pogge, R. W. 1985, ApJ, 297, 166
Page, K. L., Reeves, J. N., O'Brien, P. T., & Turner, M. J. L. 2005, MNRAS, 364, 195
Parker, M. L., Alston, W. N., Buisson, D. J. K., et al. 2017, MNRAS, 469, 1553
Parker, M. L., Reeves, J. N., Matzeu, G. A., Buisson, D. J. K., & Fabian, A. C. 2018, MNRAS, 474, 108
Pinto, C., Alston, W., Parker, M. L., et al. 2018, MNRAS, 476, 1021
Porquet, D., Reeves, J. N., O'Brien, P., et al. 2004, A&A, 422, 85
Pounds, K. A., Reeves, J. N., King, A. R., et al. 2003, MNRAS, 345, 705
Proga, D., & Kallman, T. R. 2004, ApJ, 616, 688
Reeves, J. N., Braito, V., Gofford, J., et al. 2014, ApJ, 780, 45
Reeves, J. N., O'Brien, P. T., Braito, V., et al. 2009, ApJ, 701, 493
Reeves, J. N., O'Brien, P. T., Vaughan, S., et al. 2000, MNRAS, 312, L17
Reeves, J. N., O'Brien, P. T., & Ward, M. J. 2003, ApJL, 593, L65
Reeves, J. N., & Turner, M. J. L. 2000, MNRAS, 316, 234
Saez, C., & Chartas, G. 2011, ApJ, 737, 91
Saez, C., Chartas, G., & Brandt, W. N. 2009, ApJ, 697, 194
Sargent, W. L. W. 1968, ApJL, 152, L31
Schmidt, M., & Green, R. F. 1983, ApJ, 269, 352
Scott, J. E., Kriss, G. A., Brotherton, M., et al. 2004, ApJ, 615, 135
Silk, J., & Rees, M. J. 1998, A&A, 331, L1
Silva, C. V., Costantini, E., Giustini, M., et al. 2018, MNRAS, 480, 2334
Sim, S. A., Long, K. S., Miller, L., & Turner, T. J. 2008, MNRAS, 388, 611
Sim, S. A., Miller, L., Long, K. S., Turner, T. J., & Reeves, J. N. 2010, MNRAS, 404, 1369
Sim, S. A., Proga, D., Miller, L., Long, K. S., & Turner, T. J. 2010, MNRAS, 408, 1396
Simpson, C., Ward, M., O'Brien, P., & Reeves, J. 1999, MNRAS, 303, L23
Sirressi, M., Cicone, C., Severgnini, P., et al. 2019, MNRAS, 489, 1927
Tatum, M. M., Turner, T. J., Sim, S. A., et al. 2012, ApJ, 752, 94
Tombesi, F., Cappi, M., Reeves, J. N., et al. 2010, A&A, 521, A57
Tombesi, F., Cappi, M., Reeves, J. N., et al. 2013, MNRAS, 430, 1102
Tombesi, F., Meléndez, M., Veilleux, S., et al. 2015, Natur, 519, 436
Torres, C. A. O., Quast, G. R., Coziol, R., et al. 1997, ApJL, 488, L19
Tremaine, S., Gebhardt, K., Bender, R., et al. 2002, ApJ, 574, 740
Veilleux, S., Bolatto, A., Tombesi, F., et al. 2017, ApJ, 843, 18
Veilleux, S., Meléndez, M., Sturm, E., et al. 2013, ApJ, 776, 27
Vestergaard, M., & Peterson, B. M. 2006, ApJ, 641, 689
Wilkins, D. R., Gallo, L. C., Silva, C. V., et al. 2017, MNRAS, 471, 4436
Wilms, J., Allen, A., & McCray, R. 2000, ApJ, 542, 914
Zubovas, K., & King, A. 2012, ApJL, 745, L34